

21 **3D modeling of organic haze in Pluto's**
22 **atmosphere**

23 Tanguy Bertrand ^a, François Forget ^a,

24 ^a*Laboratoire de Météorologie Dynamique, CNRS/UPMC (France)*

25 Copyright © 2005, 2006 Ross A. Beyer, David P. O'Brien, Paul Withers, and Gwen Bart

26 Number of pages: 48

27 Number of tables: 4

28 Number of figures: 12

29 **Proposed Running Head:**

30 Haze on Pluto

31 **Please send Editorial Correspondence to:**

32

33 Tanguy Bertrand

34 Laboratoire de Météorologie Dynamique, CNRS/UPMC (France)

35

36 Email: tanguy.bertrand@lmd.jussieu.fr

37

ACCEPTED MANUSCRIPT

38 **ABSTRACT**

39 The New Horizons spacecraft, which flew by Pluto on July 14, 2015, revealed
40 the presence of haze in Pluto's atmosphere that were formed by CH_4/N_2 photo-
41 chemistry at high altitudes in Pluto's atmosphere, as on Titan and Triton.
42 In order to help the analysis of the observations and further investigate the
43 formation of organic haze and its evolution at global scales, we have imple-
44 mented a simple parametrization of the formation of organic haze in our Pluto
45 General Circulation Model. The production of haze in our model is based on
46 the different steps of aerosol formation as understood on Titan and Triton:
47 photolysis of CH_4 in the upper atmosphere by Lyman- α UV radiation, pro-
48 duction of various gaseous species, and conversion into solid particles through
49 accumulation and aggregation processes. The simulations use properties of
50 aerosols similar to those observed in the detached haze layer on Titan. We
51 compared two reference simulations ran with a particle radius of 50 nm: with,
52 and without South Pole N_2 condensation. We discuss the impact of the par-
53 ticle radius and the lifetime of the precursors on the haze distribution. We
54 simulate CH_4 photolysis and the haze formation up to 600 km above the sur-
55 face. Results show that CH_4 photolysis in Pluto's atmosphere in 2015 occurred
56 mostly in the sunlit summer hemisphere with a peak at an altitude of 250 km,
57 though the interplanetary source of Lyman- α flux can induce some photolysis
58 even in the Winter hemisphere. We obtained an extensive haze up to altitudes
59 comparable with the observations, and with non-negligible densities up to 500
60 km altitude. In both reference simulations, the haze density is not strongly
61 impacted by the meridional circulation. With no South Pole N_2 condensa-
62 tion, the maximum nadir opacity and haze extent is obtained at the North
63 Pole. With South Pole N_2 condensation, the descending parcel of air above

64 the South Pole leads to a latitudinally more homogeneous haze density with
65 a slight density peak at the South Pole. The visible opacities obtained from
66 the computed mass of haze, which is about $2-4 \times 10^{-7} \text{ g cm}^{-2}$ in the summer
67 hemisphere, are similar for most of the simulation cases and in the range of
68 0.001-0.01, which is consistent with recent observations of Pluto and their
69 interpretation.

ACCEPTED MANUSCRIPT

70 *Keywords:* Pluto; Atmosphere; Haze; Modeling; GCM;

71 <http://icarus.cornell.edu/information/keywords.html>

72 1 Introduction

73 Pluto, Titan and Triton all have a nitrogen-based atmosphere containing a
74 significant fraction of methane, an efficient recipe known to lead to the forma-
75 tion of organic haze in the atmosphere, as confirmed by observations (Tomasko
76 et al., 2005; Rages and Pollack, 1992; Herbert and Sandel, 1991; Stern et al.,
77 2015) and laboratory experiments (Trainer et al., 2006; Rannou et al., 2010;
78 Lavvas et al., 2008). Here, we use the Global Climate Model of Pluto (herein re-
79 ferred to as GCM), developed at the Laboratoire de Météorologie Dynamique
80 (LMD) and designed to simulate the atmospheric circulation and the methane
81 cycle on Pluto and to investigate several aspects of the presence of haze at a
82 global scale on Pluto (Forget et al., 2016; Bertrand and Forget, 2016). What
83 controls haze formation on Pluto? At which altitudes and latitudes does it
84 form and where does sedimentation occur? What amount of particles forms
85 the haze, and what is its opacity? To address those key questions we have
86 developed a simple parametrization of haze in the GCM. The parametrization
87 is based on a function of aerosols production, which directly depends on the
88 amount of the Lyman- α UV flux. The photolysis reaction of CH_4 is photon-
89 limited. That is, all incident photons are absorbed by the CH_4 molecules
90 present in Pluto's atmosphere.

91 During the flyby of the Pluto system on July 14, 2015, the New Horizons
92 spacecraft recorded data about the structure, composition and variability of
93 Pluto's atmosphere. In particular, Alice, the UV spectrometer on-board, ob-
94 served solar occultations of Pluto's atmosphere which help to determine the
95 vertical profiles of the densities of the present atmospheric constituents and
96 provide key information about the haze. Within this context, our work aims

97 to help the analysis of the New Horizons observations with model predictions
98 of the possible evolution, spatial distribution and opacity of haze in Pluto's
99 atmosphere and on its surface.

100 We begin in Section 2 with a background on haze formation processes as
101 understood on Titan, Triton and Pluto. In Section 3 we describe the GCM. The
102 parametrization of organic haze, as well as its implementation in the model
103 are described step by step in Section 4. Finally, results are shown in Section
104 5 for two climate scenarios: with and without South Pole N₂ condensation.

105 **2 Background on planetary haze formation**

106 One of Titan's most fascinating features is the dense and widespread organic
107 haze shrouding its surface and containing a large variety of molecules which
108 strongly impact the global climate. This makes Titan a perfect place to study
109 organic chemistry and the mechanisms involved in a planetary haze forma-
110 tion. Since 2004, the exploration of Titan's haze by the Cassini/Huygens mis-
111 sion has provided a large amount of observational data, revealing complex
112 chemistry, particularly at high altitudes. This has stimulated more interest in
113 understanding this phenomenon. The haze on Titan is vertically divided into
114 two regions: a main haze up to 300 km altitude, and a thinner, overlying de-
115 tached haze typically between 400-520 km (Lavvas et al., 2009), whose origin
116 is thought to be dynamic (Rannou et al., 2002), although other scenarios were
117 suggested (Larson et al., 2015). Both layers contain solid organic material re-
118 sulting from photochemistry and microphysical mechanisms, some of which
119 remain unknown (Lebonnois et al., 2002; Wilson and Atreya, 2003; Lavvas
120 et al., 2008).

121 First, methane and nitrogen molecules are dissociated and ionized in the upper
122 atmosphere (up to 1000 km above the surface) by solar UV radiation, cosmic
123 rays and energetic electrons from Saturn's magnetosphere (Sittler et al., 2010).
124 It is commonly thought that the molecules resulting from photolysis chemi-
125 cally react with each other, which leads to the formation of larger and heav-
126 ier molecules and ions such as hydrocarbons, nitriles and oxygen-containing
127 species (Niemann et al., 2010; Cravens et al., 2006; Coates et al., 2007; Waite
128 et al., 2007; Crary et al., 2009, e.g.). While CH_4 is easily destroyed by photol-
129 ysis and provides most of the organic materials, N_2 is dissociated as well by
130 extreme UV radiation which explains the rich composition of Titan's upper
131 atmosphere. In particular, observations from Cassini and Huygens spacecrafts
132 show the presence of hydrocarbons and nitriles, such as C_2H_2 , C_2H_4 , C_2H_6 ,
133 C_4H_2 , C_6H_6 , and HCN , as well as other more complex organics (Shemansky
134 et al., 2005). These species, formed after photolysis in the upper atmosphere,
135 are the precursors of the haze. Then, through multiple processes of sedimen-
136 tation, accumulation and aggregation, the precursors are thought to turn into
137 solid organic aerosols which become heavy enough to form the orange haze
138 surrounding the moon as seen in visible wavelengths (West and Smith, 1991;
139 Rannou et al., 1995; Yelle et al., 2006; Lavvas et al., 2009). These aerosols
140 are thought to be aggregates (modeled as fractal-like particles) composed of
141 many spherical particles (monomers) that bond to each other. On Titan, the
142 aerosols start to become large enough to be visible in the detached haze layer
143 around 500 km altitude. Typically, they grow spherical up to radius 40-50 nm
144 and then form fractal particles with monomer sizes of around 50 nm (Lavvas
145 et al., 2009).

146 What are the haze's dominant pathways? What are the chemical natures of

147 complex haze particles?

148 Several microphysical models (Toon et al., 1992; Rannou et al., 1997; Lav-
149 vas et al., 2009) and photochemical models (Wilson and Atreya, 2004; Lavvas
150 et al., 2008; Hébrard et al., 2013) have been developed, combining both trans-
151 port and chemistry effects. The formation mechanisms of aerosol particles in
152 Titan's atmosphere have also been investigated using laboratory experiments.
153 By performing UV irradiation of CH₄ in a simulated Titan atmosphere, sev-
154 eral experiments have been successful in producing solid particles and have
155 found that they contain mostly high-molecular-weight organic species (e.g.,
156 Khare et al., 1984, 2002; Coll et al., 1999; Imanaka et al., 2004; Szopa et al.,
157 2006; Gautier et al., 2012). Experimental results from Trainer et al. (2006)
158 also show a linear relationship between the rate of aerosol production and the
159 rate of CH₄ photolysis. In addition, they found that an increased CH₄ con-
160 centration could lead to a decrease in aerosol production in photon-limited
161 reactions (this could be due to reactions between CH₄ and precursors forming
162 non-aerosol products).

163 Titan's atmosphere is not the unique place where organic haze can form.
164 First, similar processes of haze formation are also thought to occur on Triton
165 but yield less haze. During the Voyager 2 flyby in 1989, evidence of a thin
166 haze was detected in Triton's atmosphere from limb images taken near closest
167 approach (Smith et al., 1989; Pollack et al., 1990; Rages and Pollack, 1992)
168 and from Voyager 2 UVS solar occultation measurements (Herbert and Sandel,
169 1991; Krasnopolsky et al., 1992; Krasnopolsky, 1993). These data enabled the
170 mapping of the horizontal and vertical distribution of CH₄ and haze as well
171 as estimation of radiative and microphysical properties of the haze material.
172 Analyses showed that the haze is present nearly everywhere on Triton, from

173 the surface up to 30 km at least (Pollack et al., 1990), where it reached the limit
174 of detectability. Vertical optical depth derived from observations were found to
175 be in the range 0.01-0.03 at UV wavelength 0.15 μm , and 0.001-0.01 at visible
176 wavelength 0.47 μm . Haze particle sizes were estimated to be spherical and
177 small, around 0.1-0.2 μm (Krasnopolsky et al., 1992; Rages and Pollack, 1992;
178 Pollack et al., 1990). As on Titan, complex series of photochemical reactions
179 may be involved in the formation of this haze, starting with CH_4 photolysis by
180 the solar and the interstellar background Lyman- α radiation in the atmosphere
181 of Triton at altitudes between 50-100 km, producing hydrocarbons such as
182 C_2H_2 , C_2H_4 , C_2H_6 (Strobel et al., 1990; Krasnopolsky and Cruikshank, 1995b).
183 Dissociation of N_2 molecules is also suggested in the upper atmosphere around
184 200-500 km. Transitions between haze precursors to solid organic particles are
185 still incompletely known, but it is commonly thought that it involves similar
186 mechanisms to those on Titan. Secondly, organic chemistry has also been
187 studied in the Early Earth climate context, where a scenario of a N_2/CH_4
188 atmosphere is plausible to form a hydrocarbon haze (Trainer et al., 2006).

189 Finally, the presence of a haze on Pluto was suspected (Elliot et al., 1989;
190 Stansberry et al., 1989; Forget et al., 2014) and confirmed in 2015 by New
191 Horizons.

192 At high phase angles, Pluto's atmosphere revealed an extensive haze reaching
193 up to 200 km above the surface, composed of several layers (Stern et al., 2015).
194 Observations show that the haze is not brightest to the sub solar latitude,
195 where the incoming solar flux is stronger, but to Pluto North Pole. The haze
196 is strongly forward scattering in the visible with a blue color, while at the same
197 time there is haze extinction optical depth exceeding unity in the UV. The blue
198 color and UV extinction are consistent with a small size of about 10 nm for

	Titan	Triton	Pluto (2015)
Distance from Sun (UA)	9.5	30	32.91
Solar Flux ($\text{ph m}^{-2} \text{s}^{-1}$)	4.43×10^{13}	4.44×10^{12}	3.69×10^{12}
CH₄ mixing ratio	1.5% ^a	0.02% ^b	0.6% ^c
CO mixing ratio	0.0045%	0.07% ^b	0.05% ^c
P_{est} ($\text{kg m}^{-2} \text{s}^{-1}$)	2.94×10^{-13}	7.47×10^{-14}	5.98×10^{-14}
P_{lit} ($\text{kg m}^{-2} \text{s}^{-1}$)	$0.5 - 3 \times 10^{-13}$ ^d	6.0×10^{-14} ^e	9.8×10^{-14} ^f

^a above the tropopause, *Niemann et al. (2010)*

^b *Lellouch et al. (2010)*

^c *Lellouch et al. (2011)*

^d *Wilson and Atreya (2003); McKay et al. (2001)*

^e *Strobel and Summers (1995)*

^f *Gladstone et al. (2016)*

Table 1

Comparison of the incident UV flux and fraction of methane for a first order estimation of aerosol production rates on Titan, Triton and Pluto. The estimated rate P_{est} is compared to the observed rate P_{lit}, as detailed in the literature.

	Titan (at 400km)	Triton	Pluto
Gravity ($\text{m}^2 \text{s}^{-2}$)	1.01	0.779	0.62
Pressure (Pa)	1.5	1.4-1.9	1-1.1 ^a
Visible normal opacity	0.07 ^b	0.003-0.008 ^c	0.004 ^a

^a *Stern et al. (2015)*

^b *Cours et al. (2011)*

^c *Rages and Pollack (1992); Krasnopolsky et al. (1992)*

Table 2

Gravity, surface pressure and visible aerosol opacity on Pluto and Triton, compared to the the values encountered in the detached haze layer on Titan

199 monomers, whereas the high forward scatter to back scatter ratio in the visible
 200 suggests a much larger overall size of at least 200 nm. Although the haze may
 201 contain particles of diverse sizes and shapes depending on the altitude, these
 202 properties may also be consistent with fractal aggregate particles composed

203 of 10 nm monomers ([Gladstone et al., 2016](#); [Cheng et al., 2016](#)).

204 Although the specific mechanisms of haze formation are not fully understood,
205 it seems that the main parameters controlling the formation of haze in a
206 N_2/CH_4 atmosphere are the fractional amount of CH_4 (enough CH_4 is required
207 to avoid CH_4 -limited reactions, that is when the CH_4 concentration in the
208 atmosphere is not sufficient to absorb all incoming photons) and the UV flux
209 available to photolyze it.

210 One can compare the UV flux and the fraction of methane for Titan, Triton
211 and Pluto to estimate the haze formation rate to first order. Here we assume
212 that the impact of cosmic rays and energetic electrons from Saturn's mag-
213 netosphere is negligible for this first order comparison. As shown on Table 1
214 and Table 2, Pluto's atmosphere contains 10 times less CH_4 and receives 10
215 times less solar UV flux than Titan (relative to the atmospheric mass). Con-
216 sequently, it is likely that CH_4 photolysis on Pluto leads to the formation of
217 haze aerosols (and precursors) in lower quantities than on Titan. Compared
218 to Triton, Pluto has similar surface pressure and gravity and its atmosphere
219 contains 10 times more CH_4 , for a comparable UV flux. Thus, similar amounts
220 of haze are expected on Pluto and Triton, depending on the accelerating or
221 decelerating role of larger CH_4 amount. [Stern et al. \(2015\)](#) reported a visible
222 normal opacity of 0.004 on Pluto, which is in the range of what has been
223 observed on Triton, although it also depends on the scattering properties of
224 haze particles. On Titan, the pressure corresponding to the location of the
225 detached haze layer at about 400 km altitude is about 1 Pa, which is similar
226 to the surface pressure on Pluto in 2015. While [Rannou et al. \(2003\)](#) pre-
227 dicted the peak of production of haze in Titan's GCMs at a pressure around
228 1.5 Pa, Cassini observations ([Waite et al., 2005](#); [Teanby et al., 2012](#)) pointed

229 to active chemistry and haze formation at lower pressures. In addition, the
230 amounts of methane at these altitudes on Titan and in Pluto's atmosphere
231 are of the same order of magnitude. Thus, Pluto has sufficient pressure and
232 material in its atmosphere so that complex and opaque organic aerosols form,
233 in a manner similar to the detached haze layer on Titan. Consequently, in
234 this paper, we use the microphysical and single scattering optical properties
235 of Titan detached haze around 400 km altitude as a reference to define the
236 haze properties on Pluto while the mass of aerosols is calculated by the model
237 without any empirical assumption.

238 3 Model description

239 The LMD Pluto General Circulation Model (GCM) contains a 3D Hydrody-
240 namical core inherited and adapted from the LMD Mars GCM (Forget et al.,
241 1999). It is described in more details in Forget et al. (2016). The large-scale
242 atmospheric transport is computed through a "grid point model" composed
243 of 32 longitude and 24 latitude points. A key difference with the Forget et al.
244 (2016) version of the model is that we use 28 layers instead of 25 to extend the
245 model top up to about 600 km, with most of the layers in the first 15 km in
246 order to obtain a finer near-surface resolution, in the boundary layer. The hor-
247 izontal resolution at the equator is typically around 170 km. The physical part
248 of the model, which forces the dynamics, takes into account the N_2 and the
249 CH_4 cycles (condensation and sublimation in both the atmosphere and the
250 ground), the vertical turbulent mixing and the convection in the planetary
251 boundary layer, the radiative effect of CH_4 and CO, using the correlated-k
252 method to perform a radiative transfer run and taking into account NLTE

253 effects, a surface and subsurface thermal conduction model with 22 layers and
254 the molecular conduction and viscosity in the atmosphere.

255 4 Modeling haze on Pluto

256 Here we describe our representation of the organic haze formation and trans-
257 port in the GCM. The driving force of the photochemical reactions occurring
258 in a $\text{N}_2\text{-CH}_4$ atmospheric layer is the UV flux received by this layer. First
259 we consider the photolysis of CH_4 by Lyman- α only (Section 4.1), using the
260 results from Gladstone et al. (2015) to calculate the incident Lyman- α flux at
261 Pluto (Section 4.2). We assume that each incident photon ultimately interacts
262 with one molecule of methane, to form by photolysis haze precursors which
263 can be transported by the circulation (Section 4.3). Finally we convert haze
264 precursors into organic haze using a constant characteristic decay time (Sec-
265 tion 4.4). Haze particles properties used in this study are detailed in Section
266 4.6. In order to validate this approach, we estimate the total aerosol produc-
267 tion thus obtained on Pluto, Titan and Triton and compare with literature
268 values in Section 4.5.

269 4.1 Photolysis of CH_4 by Lyman- α

270 We consider only the photolysis of CH_4 by the Lyman- α component of the
271 UV spectrum. This is because the Hydrogen Lyman- α line at 121.6 nm is the
272 strongest ultraviolet emission line in the UV solar spectrum where absorption
273 by CH_4 happens. In fact, the solar irradiance between 0 and 160 nm (far ul-
274 traviolet) is dominated by the Lyman- α emission by a factor of 100. The UV

275 solar irradiance grows significantly at wavelengths values higher than 200 nm
 276 (middle and near-ultraviolet) but N₂, CH₄ and CO do not absorb at these
 277 wavelengths. Both N₂ and CH₄ absorb with similar efficiency in the UV but
 278 not at the same wavelengths. N₂ is the primary absorber at wavelength be-
 279 tween 10 and 100 nm, while CH₄ absorbs mainly between 100 and 145 nm.
 280 Thus the interaction between CH₄ and Lyman- α emission dominates the other
 281 interactions between the UV flux and the N₂-CH₄ atmosphere by a factor of
 282 100. On Pluto, CO may also contribute to the formation of haze. It absorbs
 283 in the far UV spectrum at similar rates that N₂. However, at 121.6 nm, it
 284 absorbs 10 times less than CH₄. Here we chose to neglect the effect of N₂ and
 285 CO absorption. This first assumption enables us to write Beer's law as the
 286 following:

$$287 \quad I(\lambda, P) = I_0 e^{-\int_0^P \frac{\sigma_{CH_4} N_a q_{CH_4}}{M_{CH_4} g} \frac{dP}{\cos(\theta)}} \quad (1)$$

288 where I_0 is the incident intensity (in $\text{ph m}^{-2} \text{s}^{-1}$) and $I(\lambda, P)$ the intensity after
 289 absorption for a given wavelength λ and pressure P , σ_{CH_4} is the absorption
 290 cross section of CH₄ at wavelength λ (here in $\text{m}^2 \text{molec}^{-1}$ but usually given in
 291 $\text{cm}^2 \text{molec}^{-1}$), q_{CH_4} is the mass mixing ratio of CH₄ at pressure P (kg kg_{air}^{-1}),
 292 M_{CH_4} is the methane molecular mass (kg mol^{-1}), N_a is the Avogadro constant,
 293 θ is the flux incident angle and g the surface gravity. We use $\sigma_{CH_4} = 1.85 \times$
 294 10^{-17} cm^2 at Lyman- α wavelength (Krasnopolsky et al., 2004) and q_{CH_4} as
 295 calculated by the GCM for each vertical layer. The calculation of the Lyman-
 296 α flux radiative transfer is performed independently for the solar and the
 297 interplanetary medium fluxes in order to take into account different values for
 298 the incident flux I_0 and the incident angle θ (see Section 4.2).

299 4.2 Sources of Lyman- α

300 The sources of Lyman- α flux at Pluto are adopted from [Gladstone et al. \(2015\)](#),
 301 which takes into account the solar as well as the interplanetary medium (IPM)
 302 Lyman- α fluxes. The IPM emission corresponds to interplanetary hydrogen
 303 atoms passing through the solar system which resonantly scatter solar Lyman-
 304 α photons and thus diffuse Lyman- α emission. Therefore the total Lyman- α
 305 flux at any pressure level P in Pluto's atmosphere is:

$$306 \quad I_{tot}(P) = I_{sol}(P) + I_{IPM}(P) \quad (2)$$

307 The solar Lyman- α flux at Pluto is inversely proportional to the square of the
 308 Sun-Pluto distance. It is obtained by considering a constant solar Lyman- α
 309 flux at Earth of 4×10^{15} ph m $^{-2}$ s $^{-1}$ and a constant extinction factor of 0.875
 310 due to the interaction with interplanetary hydrogen between Pluto and the
 311 Sun, which are values estimated by ([Gladstone et al., 2015](#)) for 2015. The
 312 solar Lyman- α flux I_0^{sol} thus estimated at Pluto is 3.23×10^{12} ph m $^{-2}$ s $^{-1}$. The
 313 incident angle θ^{sol} corresponds to the solar zenith angle.

314 The IPM Lyman- α source at Pluto is not isotropic, as shown on figure 4 in
 315 [Gladstone et al. \(2015\)](#), which presents the all-sky brightness of IPM emissions
 316 at Pluto in Rayleigh units in 2015. The brightness is stronger near the subsolar
 317 point and is minimal in the anti-sunward hemisphere. In order to take into
 318 account this property in the parametrization and compute the number of
 319 photons entering Pluto's atmosphere at a given location, we integrated the
 320 all-sky IPM brightness estimated in 2015 from [Gladstone et al. \(2015\)](#) over
 321 the half celestial sphere as seen at the considered location. The flux I_0^{IPM}
 322 obtained varies with the local time but does not strongly depend on the Sun-

323 Pluto distance (we use the flux estimated in 2015 for all other years). Figure 1
 324 shows the final result: we find a maximum flux at subsolar point of 1.15×10^{12}
 325 $\text{ph m}^{-2} \text{s}^{-1}$, a minimum flux at anti-subsolar point of $4.90 \times 10^{11} \text{ph m}^{-2} \text{s}^{-1}$ and
 326 an average flux over the planet of $7.25 \times 10^{11} \text{ph m}^{-2} \text{s}^{-1}$. We consider that the
 327 incident angle for the IPM flux θ^{IPM} is equal to the solar zenith angle during
 328 daytime, when the IPM flux is dominated by the forward scattered halo of
 329 the solar flux. When the solar zenith angle is greater than $\pi/3$ (nighttime),
 330 we consider that the IPM flux is more isotropic and we set the incident angle
 331 to $\pi/3$.

332 At the Sun-Pluto distance during New Horizon flyby (32.91 UA), this IPM
 333 source of Lyman- α is significant compared to the solar source. Considering the
 334 solar Lyman- α flux, the energy of a photon at Lyman- α wavelength (121.6 nm)
 335 and its dissipation over the whole surface of Pluto (the initial flux is divided by
 336 a factor of 4), the power of solar Lyman- α source at Pluto obtained is 22.93
 337 MW. The same calculation can be performed for the IPM flux. Gladstone
 338 [et al. \(2015\)](#) gives an averaged IPM brightness at Pluto of 145 R ($1 \text{ R} = 1/4\pi$
 339 $\times 10^{10} \text{ph m}^{-2} \text{s}^{-1} \text{sr}^{-1}$), which corresponds to a flux of $1.45 \times 10^{12} \text{ph m}^{-2} \text{s}^{-1}$
 340 once integrated on the celestial sphere. This leads to a contribution of IPM
 341 Lyman- α source at Pluto of 10.30 MW. Consequently, solar and IPM sources
 342 at Pluto account for respectively 70% and 30% of the total power source.

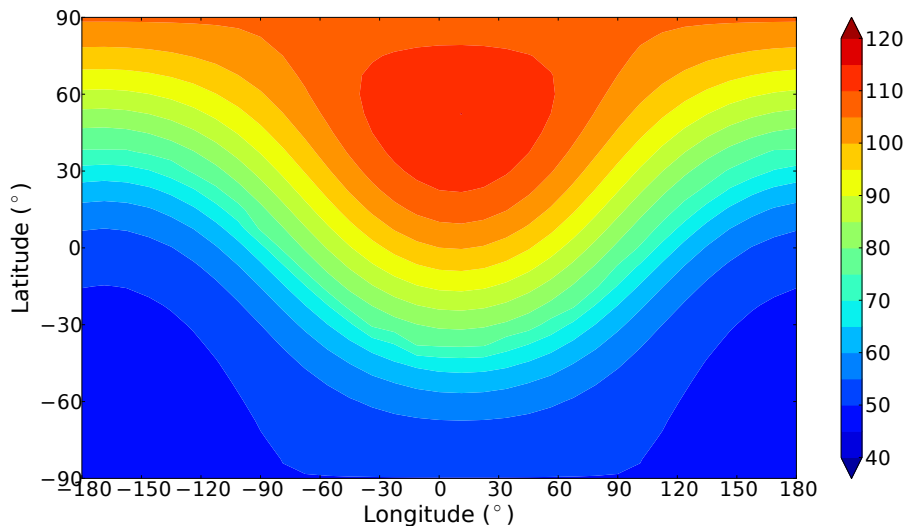


Fig. 1. An instantaneous map of interplanetary Lyman- α emission (10^{10} ph m $^{-2}$ s $^{-1}$) on Pluto in July 2015, estimated by integrating the all-sky IPM brightness given by figure 4 in Gladstone et al. (2015) over the half celestial sphere at each point of the map. In this example, the subsolar longitude is the sub Charon longitude (0°)

343 4.3 Production of haze precursors

344 In the parametrization, we consider that each absorbed Lyman- α photon de-
 345 stroys one molecule of methane by photolysis, thus forming haze precursors
 346 (CH_3 , CH_2 , $\text{CH} + \text{N}$, etc.) converted later into aerosols. Using equation 1 and
 347 2, the precursors production rate (in $\text{kg kg}_{\text{air}}^{-1} \text{s}^{-1}$) is calculated as:

$$348 \quad P_{\text{prec}}(P) = \frac{M_{\text{CH}_4} g}{N_a} \frac{dI_{\text{tot}}}{dP} \quad (3)$$

349 In the model, all possible precursors which can form during this reaction are
 350 represented by a unique gas. The equation of the reactions is:



352 This mechanisms correlates linearly the rate of haze precursors production
353 with the rate of CH_4 photolysis. It has also been used by [Trainer et al. \(2006\)](#)
354 to estimate aerosols production on Titan and Early Earth. In reality, the
355 reactions are more complex and could lead to the irreversible production of
356 HCN, or to the production of molecules such as C_2H_2 or C_2H_6 which can
357 later be photolyzed themselves as well. In addition, CH_4 molecules may be
358 chemically dissociated by reacting directly with the precursors. Consequently,
359 these reactions could lead either to an increase in the amount of carbon atoms
360 available as haze material, increasing the haze production, or to non-aerosol
361 products, slowing down the haze production ([Trainer et al., 2006](#)).

362 In the parametrization, the haze production is regulated by a factor K_{CH_4} ,
363 that corresponds to the ratio between the total number of carbon atoms in the
364 tholins and the number of carbon atoms coming from CH_4 photolysis. K_{CH_4}
365 would range from 1 to 2 (respectively all or half of the carbon in the tholins are
366 formed by direct CH_4 photolysis) if direct reactions between precursors and
367 CH_4 occur and contribute to provide tholins with carbon atoms. However, the
368 ratio could be lower than 1 considering the formation of other non-aerosol
369 products (see Section 5.3.3).

370 Additionally, nitrogen may contribute to the chemical reactions and provide
371 material for aerosol formation. In order to take into account this process, the
372 haze production is also boosted by a factor $K_N=1+N/C$, N/C representing
373 the mass ratio between nitrogen and carbon atoms contribution observed in
374 the tholins (since molar masses of nitrogen and carbon are quite similar, the
375 mass ratio is close to the number ratio). Different values of this ratio have been
376 observed in laboratory experiments, ranging from 0.25 to 1 depending on the
377 pressure (the higher the pressure, the lower the ratio), the temperature and

378 the amount of methane in the simulated atmosphere (e.g. [Coll et al., 1999](#);
379 [Tran et al., 2008](#); [Nna-Mvondo et al., 2013](#)). In the model, we adopt N/C
380 $= 0.5$, in line with the values obtained in [Nna-Mvondo et al. \(2013\)](#) at low
381 pressure, and $K_{CH_4} = 1$, so that the total production of tholins remains in
382 the range of estimated values on Titan and Pluto (see Section 4.5).

383 4.4 Conversion of haze precursors to aerosols

384 As the mechanisms at the origins of formation of organic haze are not well
385 known, another assumption is made in the parametrization: we consider that
386 the precursors become solid organic particles (by a set of processes of aggre-
387 gation and polymerization that are not represented) after a given time. In
388 practice, the amount of precursors is subject to exponential decay and is con-
389 verted into aerosols with characteristic decay time τ (or characteristic time for
390 aerosol growth). In other words, τ is the mean lifetime of the precursors be-
391 fore they become solid aerosols. This time is difficult to estimate as it depends
392 on atmospheric conditions (concentration, pressure...). However, Titan's at-
393 mospheric models show that the time needed for precursors to evolve from
394 the photolysis area to the detached layer is typically around 10^6 - 10^8 s ([Lavvas
395 et al., 2011](#); [Rammou et al., 1993](#)). Consequently, we used in our reference GCM
396 simulations a value of 10^7 s for Pluto aerosols and we examine the sensitivity
397 of the results to this parameter in Section 5.3.1.

398 Once produced, the aerosols are transported by the atmospheric circulation,
399 mixed by turbulence, and subject to gravitational sedimentation (see Section
400 4.6).

401 4.5 Discussion on total aerosol production

402 Equation 4 enables us to estimate the total haze production rate P ($\text{kg m}^{-2} \text{s}^{-1}$)
 403 in a N_2/CH_4 atmosphere:

$$404 \quad P = (F_{SOL} + F_{IPM}) \frac{M_{CH_4}}{N_a} K_{CH_4} K_N \quad \text{with} \quad F_{SOL} = \frac{I_{Earth}}{4 d_P^2} E_H \quad (5)$$

405 where F_{SOL} and F_{IPM} are the solar and IPM Lyman- α flux respectively (in
 406 $\text{ph m}^{-2} \text{s}^{-1}$), M_{CH_4} is the molar mass of methane ($M_{CH_4} = 16 \times 10^{-3} \text{ kg mol}^{-1}$),
 407 N_a is the Avogadro constant, I_{Earth} is the initial Lyman- α flux at Earth (we
 408 set $I_{Earth} = 4 \times 10^{15} \text{ ph m}^{-2} \text{s}^{-1}$), d_P is the distance in astronomical units of the
 409 considered planet P to the Sun and E_H is a constant extinction factor due to
 410 interaction with interplanetary hydrogen between the planet P and the Sun.
 411 Here E_H is set to 0.875 for the case of Pluto (Gladstone et al., 2015) and to 1
 412 for the other cases. The solar flux F_{SOL} is equal to the incident solar flux I_0^{sol}
 413 divided by a factor of 4 to take into account the distribution on the planetary
 414 sphere.

415 It is important to note that the haze production rate is independent of the CH_4
 416 concentration, even for CH_4 concentrations several orders of magnitude lower
 417 than on Pluto (see Section 5.3). The reactions are photon-limited, i.e. that
 418 enough CH_4 is present in Pluto's atmosphere for all photons to be absorbed
 419 by CH_4 .

420 In order to validate the approach described by equation 4, we apply equation
 421 5 to Titan, Triton and Pluto and compare the haze production rates obtained
 422 with the literature. The values, obtained with $K_{CH_4}=1$ and $K_N=1.5$, are sum-
 423 marized in Table 1. For Titan's case, we consider that the IPM flux is negligible

424 compared to the solar flux. Using an average Sun-Titan distance $d_{Titan}=9.5$
 425 UA, we find for Titan's atmosphere a Lyman- α flux of 1.11×10^{13} $\text{ph m}^{-2} \text{s}^{-1}$
 426 (dissipated on the planetary sphere) and a production rate of 2.94×10^{-13}
 427 $\text{kg m}^{-2} \text{s}^{-1}$. This is comparable to values found by [Wilson and Atreya \(2003\)](#)
 428 and [McKay et al. \(2001\)](#), as shown on Table 1. For Triton's case, we consider an
 429 averaged IPM flux of 340 R ([Broadfoot et al., 1989](#); [Krasnopolsky and Cruik-](#)
 430 [shank, 1995a](#)), which correspond to an IPM flux of 170×10^{10} $\text{ph m}^{-2} \text{s}^{-1}$
 431 distributed on the planetary sphere. Using an average Sun-Triton distance
 432 $d_{Titan}=30$ UA, we find for Triton's atmosphere a total Lyman- α flux (solar and
 433 IPM) of 2.81×10^{12} $\text{ph m}^{-2} \text{s}^{-1}$ and a photolysis rate of 7.47×10^{-14} $\text{kg m}^{-2} \text{s}^{-1}$,
 434 which is also in line with the literature references. Since this approach provides
 435 good estimation of Titan's and Triton's total aerosol production, we used it
 436 to estimate the aerosol production rate for Pluto's atmosphere. Equation 5
 437 gives a production rate of 5.98×10^{-14} $\text{kg m}^{-2} \text{s}^{-1}$ using the solar and IPM
 438 flux as calculated in Section 4.2. This value is one order of magnitude lower
 439 than the one on Titan (due to the UV flux one order of magnitude lower) and
 440 comparable to the value found on Triton. It is of the same order of magnitude
 441 as the value estimated on Pluto from photochemical models ([Gladstone et al.,](#)
 442 [2016](#)) shown in Table 1.

443 *4.6 Properties of haze particles for sedimentation and opacity estimations*

444 Haze precursors and particles are transported in the model by atmospheric
 445 circulation and are not radiatively active. In addition, the haze is considered
 446 too thin to affect the surface energy balance and does not change its ground
 447 albedo (in line with haze and surface observations on Triton as discussed in

448 Hillier and Veverka (1994)).

449 The density of the aerosol material in the model is set to 800 kg m^{-3} , which is
 450 in the range of values typically used on Titan (Sotin et al., 2012; Lavvas et al.,
 451 2013; Trainer et al., 2006). The size of the haze particles affects their sedi-
 452 mentation velocity and thus the haze distribution in Pluto’s atmosphere. In
 453 the GCM, we prescribe a uniform size distribution of particles. For the refer-
 454 ence simulations (with and without South Pole N_2 condensation), we assumed
 455 spherical particles with a radius of 50 nm, consistent with the properties of the
 456 detached haze layer on Titan (see Section 2). We also examine the sensitivity
 457 of the results to different sizes of particles in Section 5.3.2, in order to bracket
 458 the different possible scenarios for Pluto’s haze. We consider two lower radii
 459 of 30 nm and 10 nm, which is in the range of recent estimations (Gladstone
 460 et al., 2016), and one larger radius of 100 nm.

461 The particles fall with their Stokes velocity ω , corrected for low pressures
 462 (Rossow, 1978):

$$463 \quad \omega = \frac{2}{9} \frac{r^2 \rho g}{v} (1 + \alpha Knud) \quad \text{with} \quad Knud = \frac{k_B T}{\sqrt{2} \pi d^2 p r} \quad (6)$$

464 with r the particle radius, ρ the particle density, g the Pluto’s gravitational
 465 constant, v the viscosity of the atmosphere, $Knud$ the Knudsen number, p the
 466 considered pressure, T the atmospheric temperature, d the molecular diameter,
 467 k_B the Boltzmann’s constant and α a correction factor.

468 On Pluto, the Knudsen number is significant and thus the sedimentation veloc-
 469 ity is proportional to the particle radius. Consequently, in an ideal atmosphere
 470 without atmospheric circulation, a 100 nm particle will fall twice faster than
 471 a 50 nm particle, leading to a twice lower column mass of haze. Assuming

472 an atmospheric temperature of 100 K and a surface pressure of 1 Pa, the
473 sedimentation velocities above Pluto's surface are about 4.6×10^{-4} , 1.4×10^{-3} ,
474 2.3×10^{-3} and $4.6 \times 10^{-3} \text{ m s}^{-1}$ for an aerosol radius of 10, 30 50 and 100 nm
475 respectively.

476 One can note that the Stokes velocity is proportional to the inverse of the
477 pressure. Theoretically, the lower the pressure, the higher the sedimentation
478 velocity of the aerosol and thus the lower the mass of haze in the atmosphere.

479 The choice of the size and the shape of aerosol particles is also critical to
480 estimate their optical properties and thus their detectability. In Section 5.3.2,
481 we compare the opacities obtained with different particle radii. In Section 5.2,
482 we examine the case of fractal particles by considering that they fall at the
483 velocity of their monomers, due to their aggregate structure, which is only true
484 for a fractal dimension equal to 2 (Lavvas et al., 2011; Larson et al., 2014).

485 *4.7 Description of the reference simulations*

486 In this paper, we compare two reference simulations which correspond to the
487 two climate scenarios detailed in Forget et al. (2016): One is the case of Sputnik
488 Planum as the only reservoir of N_2 ice without N_2 condensation elsewhere
489 (referred as No South Pole N_2 condensation), and the other is the case with a
490 latitudinal band of N_2 ice at northern mid latitudes, as an additional reservoir
491 of N_2 ice with Sputnik Planum, and an initially colder South Pole, allowing
492 the N_2 ice to condense (with South Pole N_2 condensation).

493 The reference simulations study are defined as follows. A seasonal volatile
494 model of Pluto is used to simulate the ice cycles over thousands of years

495 and obtain consistent ices distribution, surface and subsurface temperatures
 496 as initial conditions for the GCM (see [Bertrand and Forget \(2016\)](#) for more
 497 details). Then, GCM runs are performed from 1988 to 2015 included so that
 498 the atmosphere has time to reach equilibrium before 2015 (the spin up time of
 499 the model is typically 10-20 Earth years). The initial conditions, the settings
 500 of the model, as well as discussions about the sensitivity of the predictions to
 501 those settings can be found in [Forget et al. \(2016\)](#).

502 The model is run with the haze parametrization using a precursor charac-
 503 teristic time for aerosol growth of 10^7 s (about 18 sols on Pluto), a fraction
 504 $K_{CH_4}=1$ and $K_N=1.5$. The density and sedimentation effective radius of haze
 505 particles are set uniformly to 800 kg m^{-3} and 50 nm respectively (see Section
 506 4.4). Table 3 summarizes the surface conditions and haze parameters used in
 507 the reference simulations ([Forget et al., 2016](#)).

508

Global Thermal Inertia ($\text{J s}^{-0.5} \text{ m}^{-2} \text{ K}^{-1}$)	50 (diurnal)	800 (seasonal)	
Albedo	0.68 (N_2 ice)	0.50 (CH_4 ice)	0.15 (Tholins)
Emissivity	0.85 (N_2 ice)	0.85 (CH_4 ice)	1 (Tholins)
Characteristic time for aerosol growth τ (s)	10^7		
K_{CH_4}	1		
K_N	1.5		
Effective radius of haze particles (nm)	50		
Density of haze particles (kg.m^{-3})	800		

Table 3

Surface conditions and settings for haze parametrization set for the GCM reference simulations

509 5 Results

510 This section presents the results obtained with the GCM coupled with the
511 haze parametrization. All figures and maps are shown using the new IAU
512 convention, spin north system for definition of the North Pole (Buie et al.,
513 1997; Zangari, 2015), that is with spring-summer in the northern hemisphere
514 during the 21th Century. Here we focus on model predictions in July 2015. We
515 first compare the two reference simulations, then we show the corresponding
516 ranges of UV and VIS opacities and we perform sensibility studies.

517 5.1 Reference simulation 1: No South Pole N_2 condensation

518 The predictions of the state of the atmosphere in July 2015 remain unchanged
519 compared to what is shown in Forget et al. (2016), since haze particles are
520 not radiatively active and since their sedimentation on Pluto's surface does
521 not impact the surface albedo. These processes could be taken into account in
522 future GCM versions.

523 In July 2015, the modeled surface pressure is found to be around 1 Pa. The
524 nitrogen reservoir in Sputnik Planum at mid northern latitudes is under sig-
525 nificant insolation during the New Horizon flyby (the subsolar latitude in July
526 2015 is 51.55° N), as well as the mid and high northern CH_4 frosts which sub-
527 lime and become an important source of atmospheric CH_4 , as described by
528 Forget et al. (2016).

529 According to equation 4, methane photolysis occurs at all latitudes but is more
530 intense at locations where strong incoming flux of Lyman- α photons occurs,

531 that is at high northern latitudes in July 2015. This is confirmed by Figure 2,
 532 showing the CH_4 photolysis rate as simulated in the GCM. All Lyman- α pho-
 533 tons are absorbed above 150 km altitude. The maximum photolysis rate is
 534 is typically around $1.3 \times 10^{-21} \text{ g cm}^{-3} \text{ s}^{-1}$ and is obtained at 250 km altitude
 535 above the North Pole.

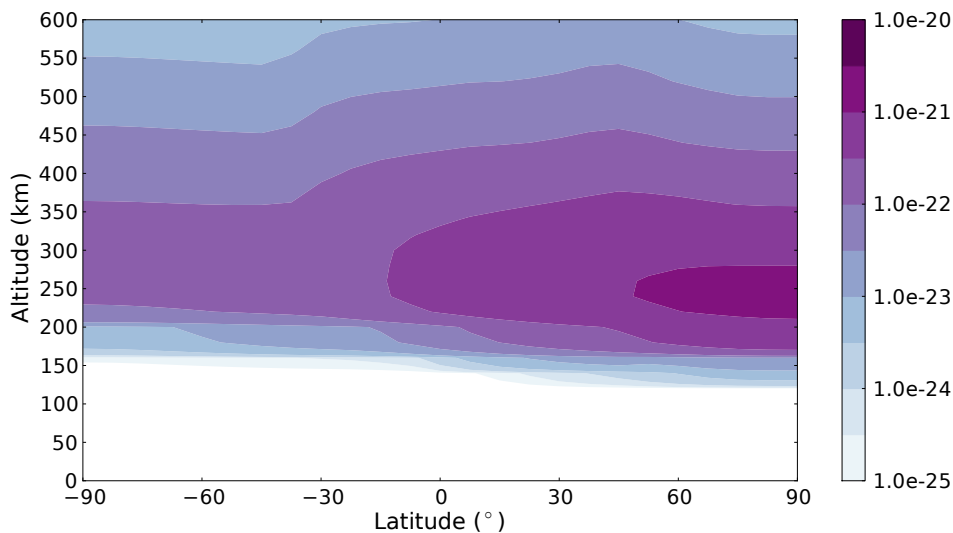


Fig. 2. Photolysis rate of CH_4 ($\text{g cm}^{-3} \text{ s}^{-1}$) obtained with the reference simulation without South Pole N_2 condensation for July 2015 (color bar in log scale)

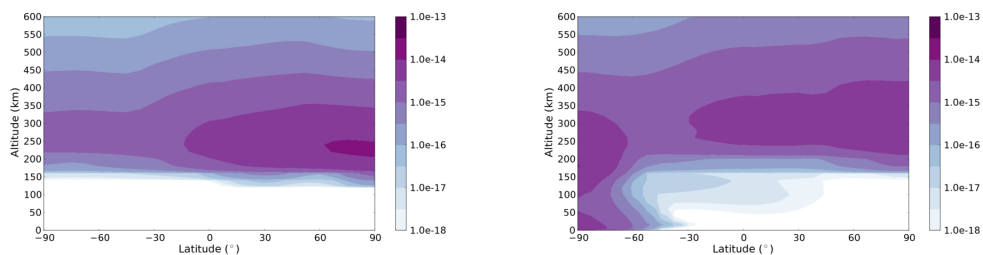


Fig. 3. Zonal mean latitudinal section of haze precursor density (g cm^{-3}) obtained with the reference simulation without (left) and with (right) South Pole N_2 condensation (color bar in log scale)

536 Haze precursors formed by CH_4 photolysis are then transported by general

537 circulation in the GCM. As shown by Forget et al. (2016), the fact that N₂
 538 ice is entirely sequestered in the Sputnik Planum basin and does not condense
 539 elsewhere leads to very low meridional wind velocities in the atmosphere and
 540 a weak meridional circulation. Consequently, haze precursors are not trans-
 541 ported fast towards the surface by circulation. In 2015, with a lifetime of 18
 542 sols, the haze precursors are still confined to high altitudes above 140 km, and
 543 are in larger amount in northern latitudes where most of the photolysis of CH₄
 544 occurs (Figure 3).

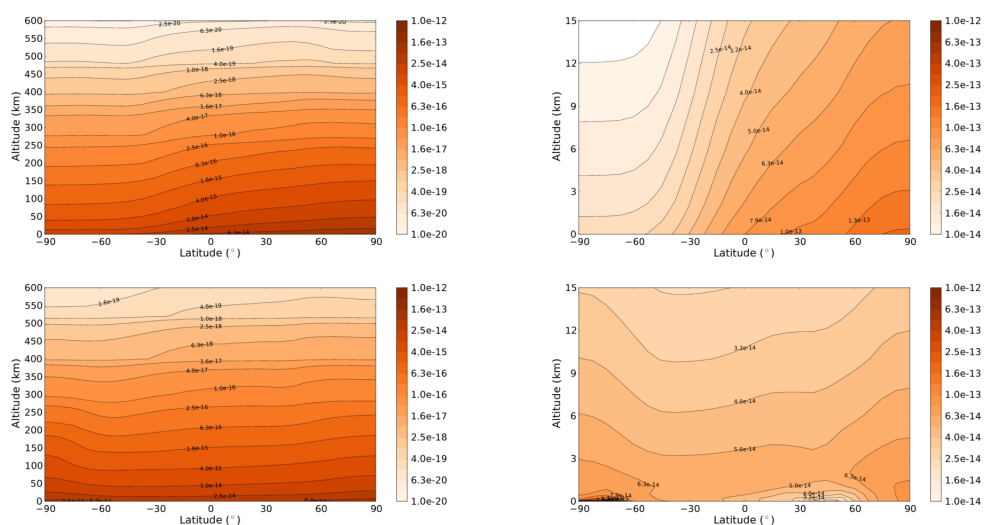


Fig. 4. Zonal mean latitudinal section of haze aerosol density (g cm^{-3}) obtained with the reference simulation for July 2015 without (top) and with (bottom) South Pole N₂ condensation (color bar in log scale). The right panels correspond to a zoom in the lowest 15 km above the surface.

545 Figure 4 shows the zonal mean latitudinal section of haze density predicted in
 546 July 2015. The aerosols formed above 150 km slowly fall towards the surface,
 547 and accumulate in the first kilometers above the surface, due to the decrease
 548 of sedimentation velocity with atmospheric pressure. The haze obtained ex-
 549 tends at high altitudes. The density decreases with the altitude but remains

550 non-negligible with values up to $4 \times 10^{-19} \text{ g cm}^{-3}$ at 500 km altitude. In this
551 case, the meridional circulation is quite weak: the diurnal condensation and
552 sublimation of N_2 ice in Sputnik region only impacts the circulation in the
553 first km above the surface, and at higher altitudes, the circulation is forced
554 by the radiative heating (the northern CH_4 warms the atmosphere, leading
555 to a transport of this warm air from the summer to the winter hemisphere)
556 inducing low meridional winds. Consequently, the general circulation does not
557 impact the haze distribution, which is dominated by the incoming flux and
558 the sedimentation velocity. In other words, the vertical and meridional at-
559 mospheric motions are not strong enough to significantly push and impact the
560 latitudinal distribution of the haze composed of 50 nm particles: the haze den-
561 sity in the atmosphere is always higher at the summer pole, where a stronger
562 CH_4 photolysis occurs.

563 In the summer hemisphere, the haze density is typically $2\text{-}4 \times 10^{-15} \text{ g cm}^{-3}$ at
564 100 km altitude while it reaches $1\text{-}2 \times 10^{-13} \text{ g cm}^{-3}$ above the surface.

565 Figure 5 shows the evolution of the mean column atmospheric mass of haze
566 aerosols since 1988. Assuming a constant initial flux of Lyman- α (at Earth)
567 and a particle radius of 50 nm, the column mass of haze reaches a peak of
568 $1.8 \times 10^{-7} \text{ g cm}^{-2}$ in 2015. Because the transport of haze is dominated by its
569 sedimentation, the column mass of haze directly depends on the sedimentation
570 velocity of the haze particles. As shown by equation 6, the sedimentation
571 velocity decreases when pressure increases, hence the increase of column mass
572 of haze, in line with the threefold increase of surface pressure since 1988.
573 Note that this trend still applies when considering the real and variable initial
574 Lyman- α flux at Earth between 1988 and 2015, as shown by Figure 5.

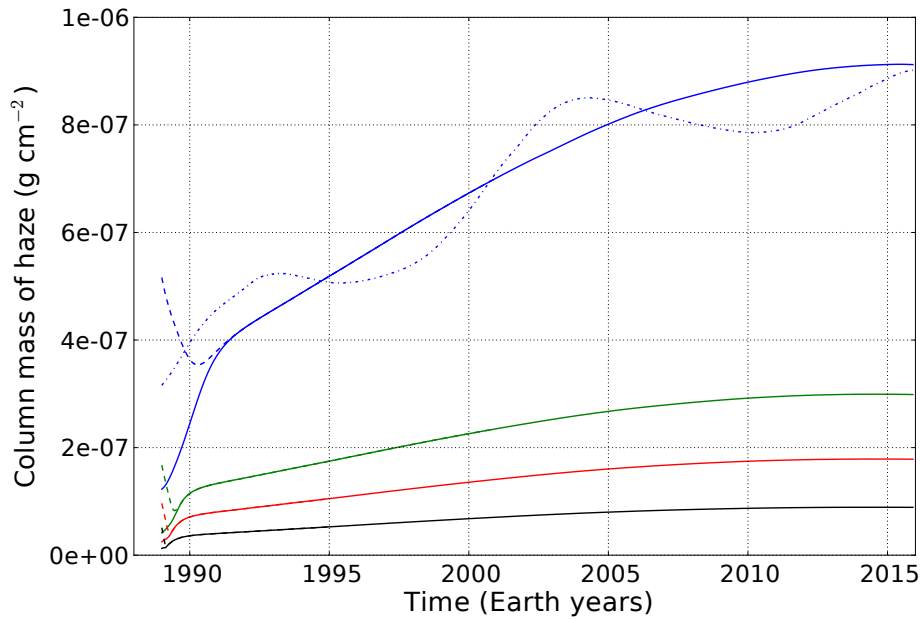


Fig. 5. Evolution of the mean column atmospheric mass of haze aerosols (g cm^{-2}) from 1988 to 2016 obtained with different particle radius in the reference simulation without South Pole N_2 condensation: 10 nm (blue), 30 nm (green), 50 nm (red) and 100 nm (black). The dashed lines correspond to similar simulations started with a higher initial amount of haze. With 50 nm particles (red curve), the mass of haze reaches an equilibrium within less than one year. The dash-dotted line corresponds to the 10 nm case with the real variable initial Lyman- α flux (at Earth).

575 Figure 6 shows the column atmospheric mass of haze aerosols. In line with
 576 the previous results, the column mass obtained is higher at the North Pole
 577 than at the South Pole by one order of magnitude, due to the maximum
 578 haze production in the summer hemisphere. The column mass of haze reaches
 579 $3.9 \times 10^{-7} \text{ g cm}^{-2}$ at the North Pole.

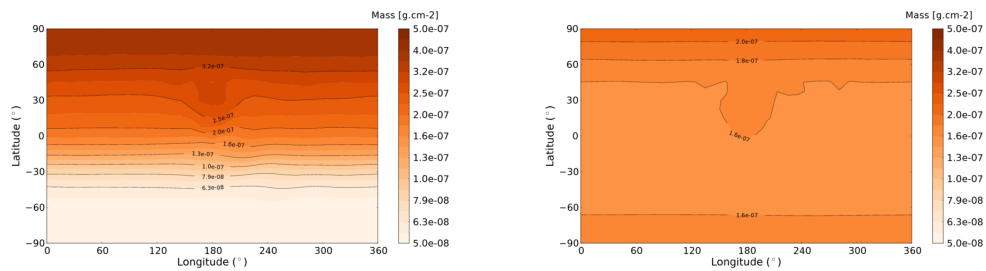


Fig. 6. Column atmospheric mass map of haze aerosols (g cm^{-2}) obtained with the reference simulation without (left) and with (right) South Pole N_2 condensation

580 5.1.1 Reference simulation 2: with South Pole N_2 condensation

581 The sublimation of N_2 in mid northern latitudes (Sputnik region and the
 582 latitudinal band) and its condensation in the winter hemisphere induce an
 583 atmospheric flow from the northern to the southern hemisphere, and thus a
 584 stronger meridional circulation than in the reference simulation without South
 585 Pole N_2 condensation, although the latitudinal winds remain relatively weak
 586 (Forget et al., 2016). Although the atmospheric methane is more mixed in
 587 the atmosphere in this case, the state of the atmosphere remains similar to
 588 the reference simulation without South Pole N_2 condensation. The surface
 589 pressure is increasing before 2015 and reaches 1 Pa in 2015.

590 Because of the condensation flow from the northern to the southern hemi-
 591 sphere, the air in the upper atmosphere is transported along with the haze
 592 precursors from the summer atmosphere to the winter atmosphere. As shown
 593 on Figure 3, the characteristic decay time of haze precursors (18 sols) is suf-
 594 ficient for some of the precursors to be transported from the summer to the
 595 winter hemisphere where the descending branch bring them at lower altitudes
 596 down to the surface.

597 As a consequence of that, more haze is formed in the winter hemisphere than
598 in the reference simulation without N₂ condensation flow, which compensates
599 the haze production in the summer hemisphere due to the higher CH₄ photoly-
600 sis rate. It leads to a similar haze density at all latitudes, as shown by Figure 4.
601 The haze density is typically 4×10^{-15} g cm⁻³ at an altitude of 100 km, which
602 is similar to the reference simulation without the condensation flow. The haze
603 remains latitudinally well dispersed down to 3 km, where the meridional cir-
604 culation driven by the N₂ condensation flow affects the haze distribution; the
605 haze is pushed towards southern latitudes by the N₂ ice sublimation above the
606 N₂ frost latitudinal band and Sputnik Planum, avoiding an accumulation of
607 haze at the mid and high northern latitudes. Between -70° S and -90° S, haze
608 particles in the first layers are suctioned towards the surface of the N₂ polar
609 cap. The haze reaches a density of about $5\text{-}20 \times 10^{-12}$ g cm⁻³ below 1 km in the
610 winter hemisphere, and $3\text{-}6 \times 10^{-14}$ g cm⁻³ in the summer hemisphere, which
611 is twice less compared to the reference simulation without the condensation
612 flow.

613 In line with the previous results, the column mass of haze in the simulation
614 with condensation flow shown on Figure 6 (right figure) is well dispersed on
615 Pluto, with small variations: in the summer atmosphere, the mass is about
616 2×10^{-7} g cm⁻², but it is slightly less at low and mid latitudes because the haze
617 above the surface is transported towards the south polar cap, and slightly more
618 at the North Pole because the haze is not impacted by the N₂ ice sublimation
619 and transport which occur at lower latitudes.

620 As in the previous simulation without South Pole N₂ condensation, the mean
621 column mass of haze increases with surface pressure. In 2015, a similar aver-
622 aged column mass of haze is obtained. Slight discrepancies are found due to

623 slightly different surface pressures to first order (Forget et al., 2016), and to
 624 the different circulation to second order.

625 5.2 Haze opacity

626 In order to better quantify the amount of haze formed on Pluto and compare
 627 with the observations as well as with the Titan and Triton cases, one can
 628 compute the total column opacity and the line of sight opacity of the haze (as a
 629 diagnostic of the results). Here we focus on the opacity at UV ($\lambda = 150$ nm) and
 630 visible ($\lambda = 550$ nm) wavelengths for sake of comparison with the data recorded
 631 by the UV spectrometer Alice and the Ralph and LORRI instruments on board
 632 New Horizons. Assuming a homogeneous size and extinction efficiency for the
 633 aerosols in Pluto's atmosphere, the opacity τ_λ for a given wavelength λ is
 634 directly proportional to the atmospheric column mass of aerosols:

$$635 \quad \tau_\lambda = \alpha \cdot M \quad \text{with} \quad \alpha = \frac{3}{4} \frac{Q_{ext,\lambda}}{\rho_{aer} r_{eff}} \quad (7)$$

636 where Q_{ext} is the aerosol extinction efficiency, r_{eff} the aerosol particle effective
 637 radius, ρ_{aer} the aerosol density and M is the atmospheric column mass of
 638 aerosol in kg m^{-2} .

639 5.2.1 Spherical particles

640 Assuming that the haze on Pluto is composed of spherical particles and be-
 641 haves like the detached haze layer on Titan, we used a Mie code to generate
 642 single scattering extinction properties for different spherical particle sizes. The
 643 code takes into account a modified gamma size distribution of particles with
 644 the considered effective radius and an effective variance $\nu_{eff} = 0.3$, as well as

645 the optical indices of [Rannou et al. \(2010\)](#). These indices have been updated
646 from [Khare et al. \(1984\)](#) thanks to new sets of Cassini observations. For 50
647 nm particles, we obtain an extinction efficiency Q_{ext} of 2.29 in UV and 0.19
648 in visible wavelengths. Using equation 7 with a density of aerosol material of
649 800 kg m^{-3} , we find that the haze column opacity in July 2015 reaches 0.077-
650 0.17 (UV) and 0.0064-0.014 (VIS) in the summer hemisphere, in the reference
651 simulation without South Pole N_2 condensation. In the simulation with South
652 Pole N_2 condensation, the opacities are 0.064-0.086 (UV) and 0.0053-0.0071
653 (VIS) in the summer hemisphere.

654 5.2.2 *Fractal particles*

655 The case of fractal particles can also be discussed. On Titan, an upper limit
656 of the maximum equivalent mass sphere radius (or bulk radius) of fractal
657 particles in the detached haze layer has been estimated to 300 nm, containing
658 up to 300 monomers ([Larson et al., 2014](#)), while larger particles containing a
659 higher number of monomers are mostly found in the main haze atmosphere
660 of Titan, at lower altitudes. In fact, some aerosols of the detached haze layer
661 on Titan are large aggregates that grow within the main haze layer at lower
662 altitudes and that are lift up back to the detached layer by ascending currents
663 occurring in the summer hemisphere ([Rannou et al., 2002](#); [Lebonnois et al.,](#)
664 [2009](#)). On Pluto, such mechanisms are not likely to occur because of the thin
665 atmosphere, and the size of fractal particles, if formed, should be limited.
666 Consequently, we consider only a small fractal particle with a limited amount
667 of monomers.

668 Fractal particles have a different optical behavior compared to spherical par-

669 ticles. As shown by the figure 10 in [Larson et al. \(2014\)](#), the optical depth
 670 of a 1 μm fractal particle is strongly dependent on the considered wavelength
 671 and decreases from the UV to the near infrared, while the optical depth of
 672 a similar sized spherical particle remains quite constant with the wavelength.
 673 One can use equation 7 to calculate the opacity of fractal particles with Q_{ext}
 674 the aerosol extinction efficiency (referred to the equivalent mass sphere), r_{eff}
 675 the equivalent mass sphere radius of the particle and ρ_{aer} the density of the
 676 material (or density of the monomers). Here we used a mean field model of
 677 scattering by fractal aggregates of identical spheres ([Botet et al., 1997](#); [Ran-](#)
 678 [nou et al., 1997](#)) to estimate the extinction efficiency of fractal particles. From
 679 the number of monomers N and the monomers radius r_m , one can calculate
 680 the equivalent mass sphere radius of the corresponding fractal particle, given
 681 by $R_s = N^{\frac{1}{3}} \times r_m$. Using these parameters and the fractal dimension of the
 682 particle, the model computes Q_{ext} by dividing the extinction cross section of
 683 the particle by the geometrical cross section of the equivalent mass sphere
 684 (πR_s^2) .

685 Here we compare the opacities obtained in the reference simulations when
 686 considering spherical or fractal particles. We consider fractal particles com-
 687 posed of 50 nm monomers, with a fractal dimension equal to 2 and with a
 688 bulk radius of 100 nm and 232 nm ($N=8$ and $N=100$ monomers respectively).
 689 The model gives an extinction efficiency Q_{ext} of 4.1 in the UV and 0.49 in the
 690 visible wavelengths for the 100 nm fractal particle and 7.2 in the UV and 1.93
 691 in the visible wavelengths for the 232 nm fractal particle. The resulting nadir
 692 opacities are summarized in Table 4 and limb opacities are shown on Figure 7.
 693 The opacities obtained for fractal particles are higher than for spherical par-
 694 ticles in the visible, with a factor of 1.3 for the 100 nm and 2.2 for the 232 nm

695 particle but lower in the UV with a factor of 0.9 and 0.7 respectively for the
696 100 nm and the 232 nm particle. This is shown by Figure 7.

697 As shown in Table 4, the visible nadir opacity obtained in the summer hemi-
698 sphere are in the range of what is estimated from New Horizons observations
699 (0.004-0.012, Stern et al. (2015); Gladstone et al. (2016)) in both the spherical
700 and the 100 nm fractal cases, and in both reference simulations. Values of the
701 232 nm fractal case are outside the observational range. The case of fractal
702 particles composed of 10 nm particles is discussed in Section 5.3.2.

703 5.2.3 Line of sight opacity profiles

704 Figure 7 shows the line of sight opacity profiles in the UV and in the visible
705 wavelengths obtained for both reference simulations at the ingress and the
706 egress points of Pluto's solar occultation by New Horizons. The profiles are
707 computed using an onion peeling method and considering that the line of
708 sight only crosses one GCM atmospheric column.

709 Generally speaking, few differences are obtained between both reference simu-
710 lations. The difference of opacity between the egress point (which is above the
711 equator at the latitude 15° N) and the ingress point (which is below the equa-
712 tor at the latitude 17° S) are larger for the simulation without South Pole N_2
713 condensation, because of the higher haze density in the summer hemisphere
714 shown in Figure 4.

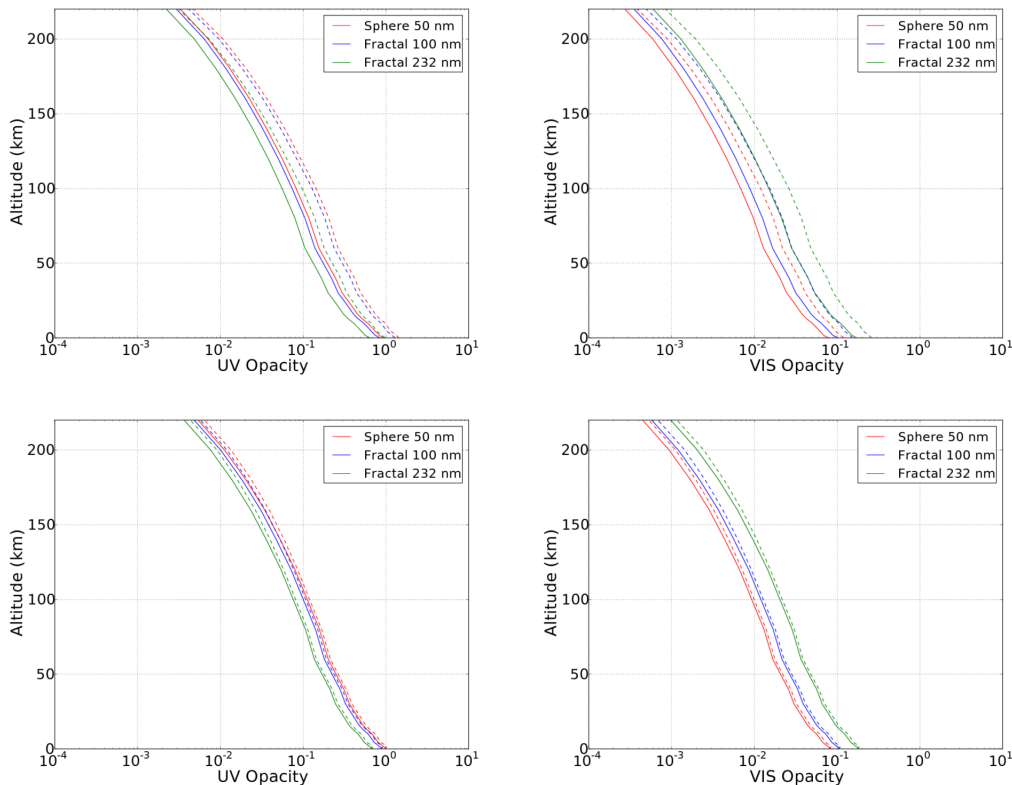


Fig. 7. Line of sight opacity profiles obtained with the GCM for the spherical and fractal cases, at the ingress (-163°E , 17°S , solid lines) and egress point (16°E , 15°N , dashed lines) of Pluto's solar occultation, for the reference simulation without (top) and with (bottom) South Pole N_2 condensation. Left and right are the results in UV and VIS wavelength respectively. The red curve is the reference simulation with 50 nm spherical particles. The blue and green curves correspond to the fractal cases with $R_s=100 \text{ nm} / N=8$ and $R_s=232 \text{ nm} / N=100$ respectively.

715 5.3 Sensitivity studies

716 The poor constraint on haze properties on Pluto gives us a flexibility to explore
 717 further other scenarios for Pluto's haze. In this section, the haze parametriza-
 718 tion is tested with different precursor lifetimes and sedimentation radius. We
 719 also discuss the possible values for K_{CH_4} in the parametrization. One objective

720 is to investigate if another set of haze parameters can cause a more realistic
721 aerosol distribution and concentration in the sunlit equatorial and summer
722 atmosphere, compared to the observations. In addition, the sensitivity study
723 aims to bracket the reality of Pluto's haze by analyzing extreme cases and
724 compare them to both reference simulations. First, it has been checked that
725 the haze production is insensitive to the amount of CH₄ present in the upper
726 atmosphere. Although the amount of CH₄ molecules decreases in the upper
727 atmosphere due to the absorption of incident photons and photolysis reac-
728 tions, this loss remains negligible compared to the total amount of CH₄ in
729 Pluto's atmosphere. In addition, the production of haze precursors still occurs
730 at high altitudes above 100 km even for low values of CH₄ mixing ratio. The
731 ratio between the production rate of precursors at 100 km and the rate at
732 220 km (top of the model) becomes higher than 1% for a mean CH₄ mixing
733 ratio of 0.04%, which is one order of magnitude less than the typical values
734 found on Pluto. This confirms that the reaction is photon-limited and that
735 different (and realistic) CH₄ mixing ratio will not impact haze production
736 and distribution.

737 *5.3.1 Sensitivity to characteristic time for aerosol growth*

738 The characteristic time for aerosol growth, defined in Section 4.4, is challeng-
739 ing to estimate. Here we consider two possible extreme values in the model.
740 If this time is set to 1 second, this means that precursors are instantaneously
741 converted into haze aerosols in the upper atmosphere where CH₄ photolysis
742 occurs. This remains acceptable since photolysis and photochemistry can ac-
743 tually occur at much higher altitudes above the model top. An upper value
744 up to several terrestrial years seems reasonable considering the number of

745 years simulated and will allow precursors to be more mixed in the entire
 746 atmosphere. Here we compare simulation results obtained with different char-
 747 acteristic times for aerosol growth (Figure 8 and Figure 9): 1 s (haze directly
 748 formed from photolysis reactions), 10^6 s (1.81 Pluto sols), 10^7 s (18.12 sols,
 749 reference simulations), 10^8 s (181.20 sols, that is about 3 terrestrials years).
 The rest of the settings remain similar to both reference simulations.

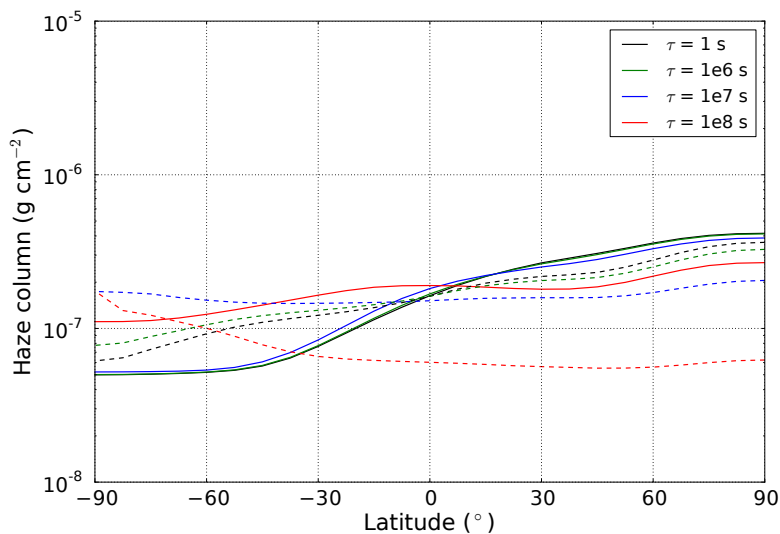


Fig. 8. Zonal mean of column atmospheric mass of haze aerosols (kg m^{-2}) obtained for July 2015 with different times for aerosol growth τ (s), for the simulations without (solid lines) and with (dashed lines) South Pole N_2 condensation.

750

751 In the simulations without South Pole N_2 condensation, using 1- 10^7 s leads to
 752 similar column mass of haze, as shown by Figure 8. With a lifetime of 10^8 s,
 753 the precursors have enough time to be transported by the circulation induced
 754 by radiative heating from the summer to the winter hemisphere, and at lower
 755 altitudes. It results in a better dispersed haze density at all latitudes, a lower
 756 mass in the summer hemisphere, and thus similar egress and ingress line of
 757 sight opacities, as shown on Figure 9.

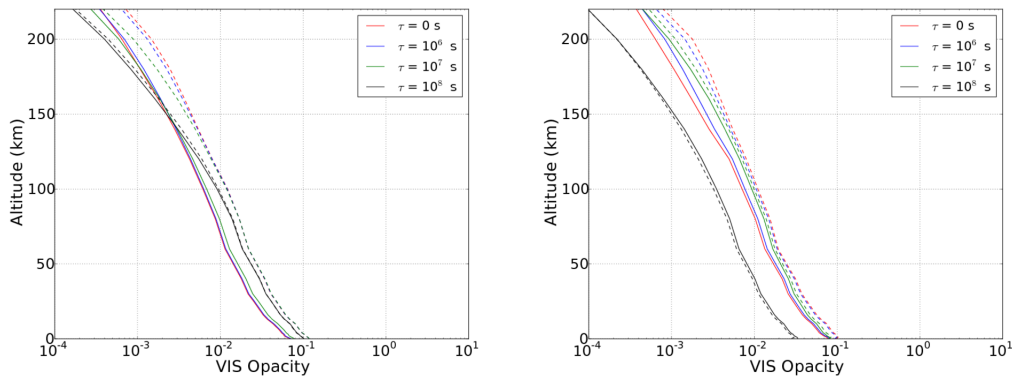


Fig. 9. Line of sight opacity profiles in VIS wavelength obtained with the GCM with different times for aerosol growth, at the ingress (-163° E , 17° S , solid lines) and egress point (16° E , 15° N , dashed lines) of Pluto's solar occultation, for the simulations without (left) and with (right) South Pole N_2 condensation

758 In the simulations with South Pole N_2 condensation, the longer the precursor
 759 lifetime, the more they are transported by radiative heating towards the win-
 760 ter hemisphere and by the descending circulation branch towards the surface
 761 of the winter polar cap. Thus, the haze tends to accumulate in the winter
 762 hemisphere and in lower amounts if long lifetimes are considered, and in the
 763 summer hemisphere in larger amounts otherwise.

764 The difference of opacity obtained between the egress and the ingress points
 765 is larger for low lifetimes and conversely, as shown on Figure 9.

766 5.3.2 Sensitivity to particle radius

767 The uniform and constant radius of aerosol particles is a parameter that
 768 strongly controls the aerosol sedimentation and opacity in the GCM. As shown
 769 by equation 6 in Section 4.6, a smaller particle radius induce a lower haze sed-
 770 imentation velocities and thus a higher mass of haze in the atmosphere. Here

771 we compare eight simulations: the reference simulations (50 nm particles, with
772 and without condensation flow) and simulations performed with particle sizes
773 of 10, 30 and 100 nm (with and without condensation flow). We compare the
774 column atmospheric mass obtained (Figure 10), the limb opacities (Figure 11)
775 and the nadir opacities (Table 4). These simulations correspond to the four
776 first lines of Table 4. The six last lines of Table 4 show the nadir opacities
777 obtained from the simulations with 10 nm and 50 nm particles, but consid-
778 ering fractal particles (four cases with 10 nm monomers and two cases with
779 50 nm monomers). Haze aerosol density is also shown for the simulation with
780 condensation flow and with a particle radius of 10 nm (Figure 12).

781 Aerosol particles with radii of 10, 30, 50 and 100 nm typically fall from 200 km
782 down to the surface in 1110, 370, 220 and 111 Earth days respectively. Ba-
783 sically, this corresponds to the time needed to reach an equilibrated mass of
784 haze in the atmosphere. As shown by Figure 10, the latitudinal mass distribu-
785 tion is not impacted by the considered size of the particle. The column mass
786 of haze is driven by the sedimentation velocity and the mass ratios correspond
787 to the particle size ratios. This is also shown by Figure 5.

788 As shown by Table 4 and Figure 11, the nadir and limb opacities remain in the
789 same order of magnitude for the simulations performed with different particle
790 radii. Lower opacities are obtained with a particle radius of 30 nm. We also
791 investigated nadir opacities for fractal particles with a bulk radius of 22, 46,
792 100 and 200 nm, respectively composed of 10, 100, 1000 and 8000 monomers
793 of 10 nm radius. As discussed in Section 2, the 200 nm fractal particle is the
794 best hypothesis for the particle shape and size in order to fit the observations.
795 Here we find that the nadir visible opacities obtained in this case are higher
796 than the upper observational limit (see Table 4). Realistic values are obtained

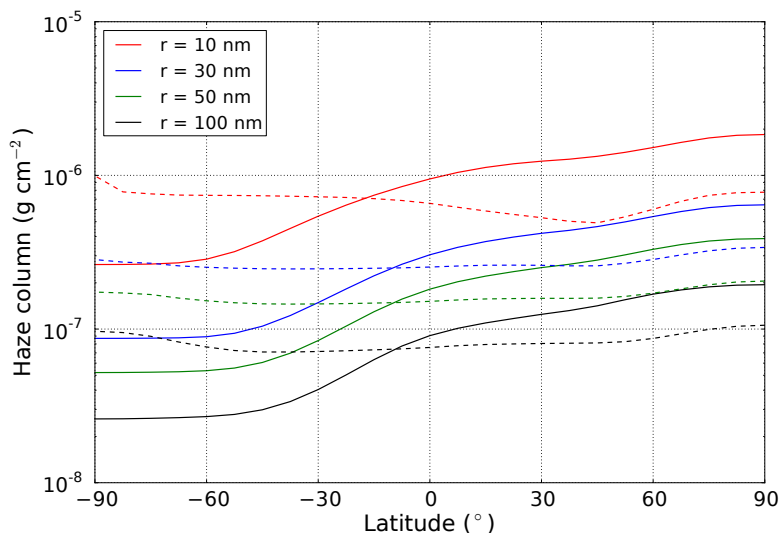


Fig. 10. Zonal mean of column atmospheric mass of haze aerosols (kg m^{-2} , log scale) obtained with different particle radii, for the simulations without (solid lines) and with (dashed lines) South Pole N_2 condensation.

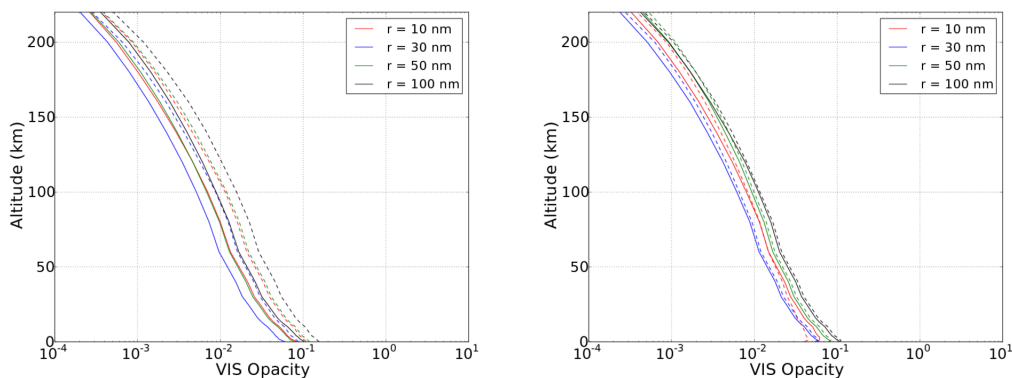


Fig. 11. Line of sight opacity profiles in VIS wavelength obtained with the GCM for different spherical particle radii, at the ingress (-163°E , 17°S , solid lines) and egress point (16°E , 15°N , dashed lines) of Pluto's solar occultation, for the simulations without (left) and with (right) South Pole N_2 condensation

797 for the other smaller particles.

798 Figure 11 show the line of sight visible opacities obtained for different spherical

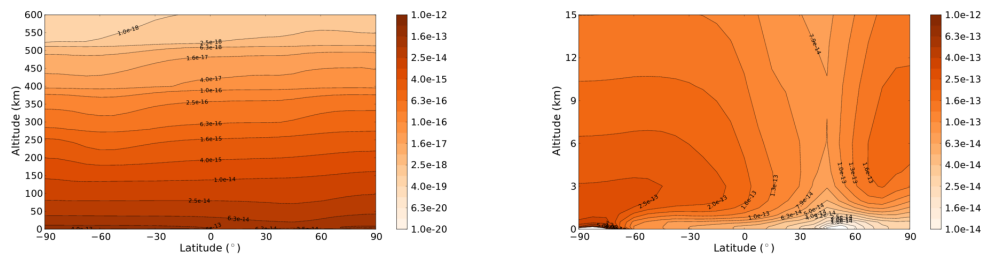


Fig. 12. Zonal mean latitudinal section of haze aerosol density (g cm^{-3}) obtained with the simulation for July 2015 with condensation flow and a particle radius of 10 nm (color bar in log scale). The right panel correspond to a zoom in the lowest 15 km above the surface.

799 particle radii. Generally speaking, the profiles have similar shapes because
 800 changing the particle radius does not affect the haze distribution but only the
 801 mass of haze in the atmosphere, due to the change of sedimentation velocity.
 802 However, for 10 nm particles, the opacities at ingress are significantly higher
 803 than at egress below 50 km, which is not the case for higher radii. This is
 804 because the particles are lighter and have more time to be transported by the
 805 circulation towards the winter hemisphere before sedimentation to the surface.
 806 Thus, the change of haze distribution due to the condensation flow below 50
 807 km altitude is more pronounced for this 10 nm case. This is highlighted by
 808 Figure 12 which shows the 10 nm haze particles density in the simulation with
 809 condensation flow. In the first kilometers above the surface, a peak of density
 810 is obtained at the South Pole. In addition, above 2 km altitude, the haze also
 811 accumulates at the North Pole, pushed away by the condensation flow.

Radius	N_m	Without winter polar cap					With winter polar cap			
		Q_{ext} UV	Q_{ext} VIS	Aerosol mass (g cm^{-2})	UV opacity	VIS opacity	Aerosol mass (g cm^{-2})	UV opacity	VIS opacity	
$r = 10 \text{ nm}$	1	0.35	0.007	$9.5 - 18 \times 10^{-7}$	0.31- 0.59	0.0062- 0.012	$4.9 - 7.8 \times 10^{-7}$	0.16- 0.26	0.0032- 0.0051	
$r = 30 \text{ nm}$	1	1.54	0.05	$3.0 - 6.5 \times 10^{-7}$	0.14- 0.31	0.0047- 0.010	$2.5 - 3.4 \times 10^{-7}$	0.12- 0.17	0.0039- 0.0053	
$r = 50 \text{ nm}$ (reference)	1	2.29	0.19	$1.8 - 3.9 \times 10^{-7}$	0.077- 0.17	0.0064- 0.014	$1.5 - 2.0 \times 10^{-7}$	0.064- 0.086	0.0053- 0.0071	
$r = 100 \text{ nm}$	1	2.67	1.01	$0.9 - 1.9 \times 10^{-7}$	0.023- 0.048	0.0085- 0.018	$0.75 - 1.1 \times 10^{-7}$	0.019- 0.028	0.0071- 0.010	
$R_s = 22 \text{ nm}$ $r = 10 \text{ nm}$	10	0.84	0.018	$9.5 - 18 \times 10^{-7}$	0.34- 0.64	0.0073- 0.014	$4.9 - 7.8 \times 10^{-7}$	0.18- 0.28	0.0038- 0.0060	
$R_s = 46 \text{ nm}$ $r = 10 \text{ nm}$	100	2.06	0.052	$9.5 - 18 \times 10^{-7}$	0.40- 0.76	0.010- 0.019	$4.9 - 7.8 \times 10^{-7}$	0.21- 0.33	0.0052- 0.0083	
$R_s = 100 \text{ nm}$ $r = 10 \text{ nm}$	1000	4.65	0.15	$9.5 - 18 \times 10^{-7}$	0.41- 0.78	0.013- 0.025	$4.9 - 7.8 \times 10^{-7}$	0.21- 0.34	0.0069- 0.0110	
$R_s = 200 \text{ nm}$ $r = 10 \text{ nm}$	8000	9.44	0.38	$9.5 - 18 \times 10^{-7}$	0.42- 0.80	0.017- 0.032	$4.9 - 7.8 \times 10^{-7}$	0.22- 0.35	0.0087- 0.0139	
$R_s = 100 \text{ nm}$ $r = 50 \text{ nm}$	8	4.10	0.49	$1.8 - 3.9 \times 10^{-7}$	0.069- 0.15	0.0083- 0.018	$1.5 - 2.0 \times 10^{-7}$	0.058- 0.077	0.0069- 0.0092	
$R_s = 232 \text{ nm}$ $r = 50 \text{ nm}$	100	7.20	1.93	$1.8 - 3.9 \times 10^{-7}$	0.052- 0.11	0.014- 0.030	$1.5 - 2.0 \times 10^{-7}$	0.044- 0.058	0.0117- 0.0156	

Table 4

Haze aerosol opacities obtained at nadir in the summer hemisphere in the GCM, for four particle radii and for both climate scenarios with and without South Pole N_2 condensation. The time for aerosol growth used is 10^7 s. The particles with a number of monomers N_m equal to 1 are spherical particles, otherwise they are fractal particles (R_s is the bulk radius, r is the monomer radius). The first four fractal particles are composed of 10 nm monomers, and the last two are composed of 50 nm monomers.

812 5.3.3 Sensitivity to the mass of aerosols

813 The haze production rate used in the reference simulations corresponds to an
814 optimal scenario where the photolysis of one molecule of CH_4 gives one carbon
815 atom available for the production of haze ($K_{\text{CH}_4}=1$). However, the carbon

816 atoms collected from CH_4 photolysis may form different gaseous species and
817 slow down tholins production. As an example, [McKay et al. \(2001\)](#) suggest that
818 the tholins production is about 25 less than the photolysis rate of methane.
819 Therefore, lower values of K_{CH_4} remain possible and would lead to a decrease
820 of aerosol mass and thus of opacity.

821 **6 Summary**

822 The parametrization of haze aerosols in the Pluto GCM consists of several
823 steps: the photolysis of methane by the solar and IPM flux, the creation of haze
824 precursors and their transport in the atmosphere, the conversion of precursors
825 to haze aerosols and the sedimentation of the aerosols. The haze parametriza-
826 tion has been tested with 50 nm particles, a time for aerosol growth of 10^7 s,
827 and for the two climate scenarios described in [Forget et al. \(2016\)](#): with and
828 without South Pole N_2 condensation (reference simulations). The sensitivity
829 of the model to other particle sizes and times for aerosol growth has been
830 explored. Results show that the CH_4 photolysis occurs at all latitudes, with a
831 maximum rate at high northern latitudes and around 250 km in altitude. In
832 all simulations, the haze extends to high altitudes, comparable to what has
833 been observed by New Horizons. From 200 km altitude upwards, the density
834 decreases with the altitude by one order of magnitude every 100 km, leading
835 to a density scale height of typically 40 km above 60 km altitude. This is com-
836 parable to the typical haze brightness scale height of 50 km observed by New
837 Horizons ([Gladstone et al., 2016](#)). Without South Pole N_2 condensation, the
838 meridional atmospheric circulation is dominated by the radiative heating but
839 remains weak, even in the first kilometers above the surface. The haze precur-

sors remains at high altitudes and in larger amount at high northern latitudes. This leads to a higher density of haze in the summer hemisphere, decreasing with the latitudes. With South Pole N_2 condensation, the circulation is also weak in the upper atmosphere, except above the South Pole where a descending branch of air driven by the condensation of N_2 transports the precursors to lower altitudes. This leads to a distribution of haze latitudinally more homogeneous with a slight peak of haze density above the South Pole. This peak is reinforced by the circulation in the first kilometers above the surface, which is more intense and able to move light aerosols from the northern hemisphere towards the South Pole. In both climate scenarios, because of the generally weak meridional circulation, the computed mean atmospheric column mass of haze remains similar, and primarily depends on the sedimentation velocity and thus on the pressure and the considered monomer radius. In our simulations, the initial flux of Lyman- α at Earth remains constant between 1990 and 2015, but even if we consider the variable initial flux of Lyman- α , the flux of Lyman- α at Pluto remains relatively constant. Consequently, the mean column mass of haze follows the trend in surface pressure, that is an increase by a factor of 3 between 1990 and 2015. Haze particles with a small radius remain longer in the atmosphere before reaching the surface. In our simulations, the sedimentation fall of 10 nm particles lasts about 3 terrestrial years, which could be enough time to form fractal aggregates. The mean column atmospheric mass of haze on Pluto is difficult to assess because it depends on many parameters. First, it is depending on the photolysis rate and the complex recombinations of carbon and nitrogen atoms. The parametrization uses K_{CH_4} and K_N equal to 1 and 1.5 to take these mechanisms into account. However, the production could be overestimated. In fact, New Horizons detected the presence of C_2H_2 , C_2H_4 and maybe other carbon-based gas in Pluto atmosphere, which

867 suggests another pathway for carbon atoms formed by CH_4 photolysis. In ad-
868 dition, HCN has been detected, and the irreversible nature of its formation
869 may lead to less nitrogen atoms available for the haze formation. The column
870 mass of haze also strongly depends on the sedimentation radius of the haze
871 particle, and to a lesser extent on the lifetime of the haze precursors. How-
872 ever, we computed the UV and VIS opacities of the haze as a diagnostic of
873 our simulation results and in all simulation cases, the column visible opacities
874 have similar values (same order of magnitude) around 0.001-0.01, and slightly
875 higher values when considering large fractal particles. This is because the ex-
876 tinction factor of smaller particles is lower but is compensated by a larger
877 mass of haze. These opacities are in the range of what has been estimated
878 on Pluto, that is 0.003-0.012 (Gladstone et al., 2016; Stern et al., 2015), and
879 thus suggest an acceptable order of magnitude for the mass of haze obtained.
880 Comparing the haze distribution (obtained with and without South Pole N_2
881 condensation) with the observations (made by imaging with the instruments
882 Ralph/MVIC and LORRI and by UV occultation with the Alice spectrom-
883 eter) can help to reveal the presence or the absence of N_2 ice at the South
884 Pole. A latitudinally homogeneous haze density with a slight peak above the
885 North and particularly above the South Pole is typical of our simulation with
886 South Pole N_2 condensation. Conversely, simulations without South Pole N_2
887 condensation show a more extensive haze in the summer hemisphere. Com-
888 paring the line of sight opacity profiles at the egress and the ingress points
889 can also help to distinguish both cases. The opacity at the egress point is at
890 least twice the opacity at the ingress point in the case without South Pole
891 N_2 condensation, and no significant difference is obtained in the case without.
892 However, a latitudinally homogeneous haze density can also be the results of a
893 long characteristic time for precursors growth (several terrestrial years), that

894 allows precursors to be transported towards southern latitudes by radiative
895 heating and meridional circulation. Finally, another way to distinguish both
896 cases is to compare the haze distribution in the first kilometers above the
897 surface. Figure 12 shows that the condensation flow induced by the presence
898 of N_2 ice in the winter hemisphere leads to a lack of haze above the surface
899 in the summer hemisphere, and an accumulation of haze between 3 and 20
900 kilometers in the winter hemisphere, which is more pronounced for small par-
901 ticle radii. Although the simulations were done with uniform particle sizes, in
902 reality the haze particle size may be locally distributed and vary in space and
903 time, especially in the vertical. Thus it may be more realistic to consider a dis-
904 tribution of haze particle sizes, in order to take into account the gravitational
905 segregation. Compared to the uniform size case, if 10 nm spherical particles in
906 the upper atmosphere become fractal particles in the lower atmosphere, with
907 same monomer radius, then there will be a change in opacity but not in haze
908 vertical distribution (because the sedimentation velocity remains the same).
909 If 10 nm spherical particles grow up to 100 nm during their fall down towards
910 the surface, then the sedimentation velocity of the particle would change. The
911 increase of the particle size during the fall would compensate the increase of
912 atmospheric pressure and lead to a more homogeneous haze density with al-
913 titude. In addition, at the altitudes where transitions of particle size occur,
914 layers of haze could form.

915 **Acknowledgements**

916 We wish to thank P. Rannou and E. Lellouch for helpful conversations and
917 suggestions. We are grateful to P. Rannou for supplying a mean model of

918 absorption and scattering by fractal particles of identical spheres. The authors
919 thank the NASA *New Horizons* team for their excellent work on a fantastic
920 mission and their interest in this research.

921 References

922 T. Bertrand and F. Forget. Observed glacier and volatile distribution on Pluto
923 from atmospheretopography processes. *Nature*, 987, September 2016. doi:
924 10.1038/nature19337.

925 Robert Botet, Pascal Rannou, and Michel Cabane. Mean-field approximation
926 of mie scattering by fractal aggregates of identical spheres. *Appl. Opt.*, 36
927 (33):8791–8797, Nov 1997. doi: 10.1364/AO.36.008791. URL [http://ao.
928 osa.org/abstract.cfm?URI=ao-36-33-8791](http://ao.osa.org/abstract.cfm?URI=ao-36-33-8791).

929 A. L. Broadfoot, S. K. Atreya, J. L. Bertaux, J. E. Blamont, A. J. Dessler,
930 T. M. Donahue, W. T. Forrester, D. T. Hall, F. Herbert, J. B. Holberg, D. M.
931 Hunten, V. A. Krasnopolsky, S. Linick, J. I. Lunine, J. C. McConnell, H. W.
932 Moos, B. R. Sandel, N. M. Schneider, D. E. Shemansky, G. R. Smith, D. F.
933 Strobel, and R. V. Yelle. Ultraviolet spectrometer observations of Neptune
934 and Triton. *Science*, 246:1459–1466, December 1989. doi: 10.1126/science.
935 246.4936.1459.

936 M. W. Buie, D. J. Tholen, and L. H. Wasserman. Separate Lightcurves of
937 Pluto and Charon. *Icarus*, 125:233–244, February 1997. doi: 10.1006/icar.
938 1996.5624.

939 A. F. Cheng, M. E. Summers, G. R. Gladstone, D. F. Strobel, L. A. Young,
940 P. Lavvas, J. A. Kammer, C. M. Lisse, A. H. Parker, E. F. Young, S. A.
941 Stern, H. A. Weaver, C. B. Olkin, and K. Ennico. Haze Layers in Pluto's
942 Atmosphere. In *Lunar and Planetary Science Conference*, volume 47 of

- 943 *Lunar and Planetary Science Conference*, page 2316, March 2016.
- 944 A. J. Coates, F. J. Crary, G. R. Lewis, D. T. Young, J. H. Waite, and
945 E. C. Sittler. Discovery of heavy negative ions in Titan's ionosphere. *Geo-*
946 *phys. Res. Lett.*, 34:L22103, November 2007. doi: 10.1029/2007GL030978.
- 947 P. Coll, D. Coscia, N. Smith, M.-C. Gazeau, S. I. Ramírez, G. Cernogora,
948 G. Israël, and F. Raulin. Experimental laboratory simulation of Titan's
949 atmosphere: aerosols and gas phase. *Planet. Space Sci.*, 47:1331–1340, Oc-
950 tober 1999. doi: 10.1016/S0032-0633(99)00054-9.
- 951 T. Cours, J. Burgalat, P. Rannou, S. Rodriguez, A. Brahic, and R. A. West.
952 Dual Origin of Aerosols in Titan's Detached Haze Layer. *ApJ*, 741:L32,
953 November 2011. doi: 10.1088/2041-8205/741/2/L32.
- 954 F. J. Crary, B. A. Magee, K. Mandt, J. H. Waite, J. Westlake, and D. T.
955 Young. Heavy ions, temperatures and winds in Titan's ionosphere: Com-
956 bined Cassini CAPS and INMS observations. *Planet. Space Sci.*, 57:1847–
957 1856, December 2009. doi: 10.1016/j.pss.2009.09.006.
- 958 T. E. Cravens, I. P. Robertson, J. H. Waite, R. V. Yelle, W. T. Kasprzak,
959 C. N. Keller, S. A. Ledvina, H. B. Niemann, J. G. Luhmann, R. L. McNutt,
960 W.-H. Ip, V. De La Haye, I. Mueller-Wodarg, J.-E. Wahlund, V. G. Anicich,
961 and V. Vuitton. Composition of Titan's ionosphere. *Geophys. Res. Lett.*,
962 33:L07105, April 2006. doi: 10.1029/2005GL025575.
- 963 J. L. Elliot, E. W. Dunham, A. S. Bosh, S. M. Slivan, L. A. Young, L. H.
964 Wasserman, and R. L. Millis. Pluto's atmosphere. *Icarus*, 77:148–170, Jan-
965 uary 1989. doi: 10.1016/0019-1035(89)90014-6.
- 966 F. Forget, F. Hourdin, R. Fournier, C. Hourdin, O. Talagrand, M. Collins, S. R.
967 Lewis, P. L. Read, and J.-P. Huot. Improved general circulation models of
968 the Martian atmosphere from the surface to above 80 km. *J. Geophys. Res.*,
969 104:24155–24176, October 1999. doi: 10.1029/1999JE001025.

- 970 F. Forget, M. Vangvichith, and T. Bertrand. What will Pluto's atmosphere
971 look like ? Predictions from a Global Climate Model including the methane
972 cycle. *AGU Fall Meeting Abstracts*, December 2014.
- 973 F. Forget, T. Bertrand, M. Vangvichith, J. Leconte, E. Millour, and E. Lel-
974 louch. A post-New Horizons Global climate model of the Pluto system
975 including the N₂, CH₄ and CO cycle - submitted to *Icarus*. *Icarus*, 2016.
- 976 T. Gautier, N. Carrasco, A. Mahjoub, S. Vinatier, A. Giuliani, C. Szopa, C. M.
977 Anderson, J.-J. Correia, P. Dumas, and G. Cernogora. Mid- and far-infrared
978 absorption spectroscopy of Titan's aerosols analogues. *Icarus*, 221:320–327,
979 September 2012. doi: 10.1016/j.icarus.2012.07.025.
- 980 G. Gladstone, W. R. Pryor, and S. Alan Stern. Ly α @Pluto. *Icarus*, 246:
981 279–284, January 2015. doi: 10.1016/j.icarus.2014.04.016.
- 982 G. R. Gladstone, S. A. Stern, K. Ennico, C. B. Olkin, H. A. Weaver, L. A.
983 Young, M. E. Summers, D. F. Strobel, D. P. Hinson, J. A. Kammer, A. H.
984 Parker, A. J. Steffl, I. R. Linscott, J. W. Parker, A. F. Cheng, D. C. Slater,
985 M. H. Versteeg, T. K. Greathouse, K. D. Retherford, H. Throop, N. J. Cun-
986 ningham, W. W. Woods, K. N. Singer, C. C. C. Tsang, E. Schindhelm,
987 C. M. Lisse, M. L. Wong, Y. L. Yung, X. Zhu, W. Curdt, P. Lavvas, E. F.
988 Young, G. L. Tyler, F. Bagenal, W. M. Grundy, W. B. McKinnon, J. M.
989 Moore, J. R. Spencer, T. Andert, J. Andrews, M. Banks, B. Bauer, J. Bau-
990 man, O. S. Barnouin, P. Bedini, K. Beisser, R. A. Beyer, S. Bhaskaran,
991 R. P. Binzel, E. Birath, M. Bird, D. J. Bogan, A. Bowman, V. J. Bray,
992 M. Brozovic, C. Bryan, M. R. Buckley, M. W. Buie, B. J. Buratti, S. S.
993 Bushman, A. Calloway, B. Carcich, S. Conard, C. A. Conrad, J. C. Cook,
994 D. P. Cruikshank, O. S. Custodio, C. M. D. Ore, C. Deboy, Z. J. B. Dischner,
995 P. Dumont, A. M. Earle, H. A. Elliott, J. Ercol, C. M. Ernst, T. Finley, S. H.
996 Flanigan, G. Fountain, M. J. Freeze, J. L. Green, Y. Guo, M. Hahn, D. P.

- 997 Hamilton, S. A. Hamilton, J. Hanley, A. Harch, H. M. Hart, C. B. Hersman,
998 A. Hill, M. E. Hill, M. E. Holdridge, M. Horanyi, A. D. Howard, C. J. A.
999 Howett, C. Jackman, R. A. Jacobson, D. E. Jennings, H. K. Kang, D. E.
1000 Kaufmann, P. Kollmann, S. M. Krimigis, D. Kusnierkiewicz, T. R. Lauer,
1001 J. E. Lee, K. L. Lindstrom, A. W. Lunsford, V. A. Mallder, N. Martin, D. J.
1002 McComas, R. L. McNutt, D. Mehoke, T. Mehoke, E. D. Melin, M. Mutchler,
1003 D. Nelson, F. Nimmo, J. I. Nunez, A. Ocampo, W. M. Owen, M. Paetzold,
1004 B. Page, F. Pelletier, J. Peterson, N. Pinkine, M. Piquette, S. B. Porter,
1005 S. Protopapa, J. Redfern, H. J. Reitsema, D. C. Reuter, J. H. Roberts, S. J.
1006 Robbins, G. Rogers, D. Rose, K. Runyon, M. G. Ryschkewitsch, P. Schenk,
1007 B. Sepan, M. R. Showalter, M. Soluri, D. Stanbridge, T. Stryk, J. R. Szalay,
1008 M. Tapley, A. Taylor, H. Taylor, O. M. Umurhan, A. J. Verbiscer, M. H.
1009 Versteeg, M. Vincent, R. Webbert, S. Weidner, G. E. Weigle, O. L. White,
1010 K. Whittenburg, B. G. Williams, K. Williams, S. Williams, A. M. Zangari,
1011 and E. Zirnstein. The atmosphere of Pluto as observed by New Horizons.
1012 *Science*, 351:aad8866, March 2016. doi: 10.1126/science.aad8866.
- 1013 E. Hébrard, M. Dobrijevic, J. C. Loison, A. Bergeat, K. M. Hickson, and
1014 F. Caralp. Photochemistry of C_3H_p hydrocarbons in Titan's stratosphere
1015 revisited. *A&A*, 552:A132, April 2013. doi: 10.1051/0004-6361/201220686.
- 1016 F. Herbert and B. R. Sandel. CH_4 and haze in Triton's lower atmosphere.
1017 *J. Geophys. Res.*, 96:19241, October 1991.
- 1018 J. Hillier and J. Veverka. Photometric properties of Triton hazes. *Icarus*, 109:
1019 284–295, June 1994. doi: 10.1006/icar.1994.1094.
- 1020 H. Imanaka, B. N. Khare, J. E. Elsila, E. L. O. Bakes, C. P. McKay, D. P.
1021 Cruikshank, S. Sugita, T. Matsui, and R. N. Zare. Laboratory experiments
1022 of Titan tholin formed in cold plasma at various pressures: implications for
1023 nitrogen-containing polycyclic aromatic compounds in Titan haze. *Icarus*,

- 1024 168:344–366, April 2004. doi: 10.1016/j.icarus.2003.12.014.
- 1025 B. N. Khare, C. Sagan, W. R. Thompson, E. T. Arakawa, F. Suits, T. A.
1026 Callcott, M. W. Williams, S. Shrader, H. Ogino, T. O. Willingham, and
1027 B. Nagy. The organic aerosols of Titan. *Advances in Space Research*, 4:
1028 59–68, 1984. doi: 10.1016/0273-1177(84)90545-3.
- 1029 B. N. Khare, E. L. O. Bakes, H. Imanaka, C. P. McKay, D. P. Cruikshank,
1030 and E. T. Arakawa. Analysis of the Time-Dependent Chemical Evolution
1031 of Titan Haze Tholin. *Icarus*, 160:172–182, November 2002. doi: 10.1006/
1032 icar.2002.6899.
- 1033 V. A. Krasnopolsky. On the haze model for Triton. *J. Geophys. Res.*, 98:
1034 17123–17124, September 1993. doi: 10.1029/93JE01459.
- 1035 V. A. Krasnopolsky and D. P. Cruikshank. Photochemistry of Triton’s Atmo-
1036 sphere and Ionosphere. *J. Geophys. Res.*, 100:11271, October 1995a.
- 1037 V. A. Krasnopolsky and D. P. Cruikshank. Photochemistry of Triton’s at-
1038 mosphere and ionosphere. *J. Geophys. Res.*, 100:21271–21286, 1995b. doi:
1039 10.1029/95JE01904.
- 1040 V. A. Krasnopolsky, B. R. Sandel, and F. Herbert. Properties of haze in
1041 the atmosphere of Triton. *J. Geophys. Res.*, 97:11695, July 1992. doi:
1042 10.1029/92JE00945.
- 1043 V. A. Krasnopolsky, J. P. Maillard, and T. C. Owen. Detection of methane in
1044 the martian atmosphere: evidence for life? *Icarus*, 172:537–547, December
1045 2004. doi: 10.1016/j.icarus.2004.07.004.
- 1046 E. J. L. Larson, O. B. Toon, and A. J. Friedson. Simulating Titan’s aerosols in
1047 a three dimensional general circulation model. *Icarus*, 243:400–419, Novem-
1048 ber 2014. doi: 10.1016/j.icarus.2014.09.003.
- 1049 E. J. L. Larson, O. B. Toon, R. A. West, and A. J. Friedson. Microphysical
1050 modeling of Titan’s detached haze layer in a 3D GCM. *Icarus*, 254:122–134,

- 1051 July 2015. doi: 10.1016/j.icarus.2015.03.010.
- 1052 P. Lavvas, R. V. Yelle, and V. Vuitton. The detached haze layer in Titan's
1053 mesosphere. *Icarus*, 201:626–633, June 2009. doi: 10.1016/j.icarus.2009.01.
1054 004.
- 1055 P. Lavvas, M. Sander, M. Kraft, and H. Imanaka. Surface Chemistry and Par-
1056 ticle Shape: Processes for the Evolution of Aerosols in Titan's Atmosphere.
1057 *ApJ*, 728:80, February 2011. doi: 10.1088/0004-637X/728/2/80.
- 1058 P. P. Lavvas, A. Coustenis, and I. M. Vardavas. Coupling photochemistry
1059 with haze formation in Titan's atmosphere, Part II: Results and validation
1060 with Cassini/Huygens data. *Planet. Space Sci.*, 56:67–99, January 2008.
1061 doi: 10.1016/j.pss.2007.05.027.
- 1062 Panayotis Lavvas, Roger V. Yelle, Tommi Koskinen, Axel Bazin, Veronique
1063 Vuitton, Erik Vigren, Marina Galand, Anne Wellbrock, Andrew J. Coates,
1064 Jan-Erik Wahlund, Frank J. Crary, and Darci Snowden. Aerosol growth in
1065 titan's ionosphere. *Proceedings of the National Academy of Sciences of the*
1066 *United States of America*, 110(8):2729–2734, 2013.
- 1067 S. Lebonnois, E. L. O. Bakes, and C. P. McKay. Transition from Gaseous
1068 Compounds to Aerosols in Titan's Atmosphere. *Icarus*, 159:505–517, Octo-
1069 ber 2002. doi: 10.1006/icar.2002.6943.
- 1070 S. Lebonnois, P. Rannou, and F. Hourdin. The coupling of winds, aerosols
1071 and chemistry in Titan's atmosphere. *Royal Society of London Philosophical*
1072 *Transactions Series A*, 367:665–682, February 2009. doi: 10.1098/rsta.2008.
1073 0243.
- 1074 E. Lellouch, C. de Bergh, B. Sicardy, S. Ferron, and H.-U. Käuffl. Detection
1075 of CO in Triton's atmosphere and the nature of surface-atmosphere inter-
1076 actions. *A&A*, 512:L8, March 2010. doi: 10.1051/0004-6361/201014339.
- 1077 E. Lellouch, J. Stansberry, J. Emery, W. Grundy, and D. P. Cruikshank. Ther-

- 1078 mal properties of Pluto's and Charon's surfaces from Spitzer observations.
1079 *Icarus*, 214:701–716, August 2011. doi: 10.1016/j.icarus.2011.05.035.
- 1080 C. P. McKay, A. Coustenis, R. E. Samuelson, M. T. Lemmon, R. D. Lorenz,
1081 M. Cabane, P. Rannou, and P. Drossart. Physical properties of the organic
1082 aerosols and clouds on Titan. *Planet. Space Sci.*, 49:79–99, January 2001.
1083 doi: 10.1016/S0032-0633(00)00051-9.
- 1084 H. B. Niemann, S. K. Atreya, J. E. Demick, D. Gautier, J. A. Haberman, D. N.
1085 Harpold, W. T. Kasprzak, J. I. Lunine, T. C. Owen, and F. Raulin. Compo-
1086 sition of Titan's lower atmosphere and simple surface volatiles as measured
1087 by the Cassini-Huygens probe gas chromatograph mass spectrometer exper-
1088 iment. *Journal of Geophysical Research (Planets)*, 115:E12006, December
1089 2010. doi: 10.1029/2010JE003659.
- 1090 D. Nna-Mvondo, J. L. de la Fuente, M. Ruiz-Bermejo, B. Khare, and C. P.
1091 McKay. Thermal characterization of Titan's tholins by simultaneous TG-
1092 MS, DTA, DSC analysis. *Planet. Space Sci.*, 85:279–288, September 2013.
1093 doi: 10.1016/j.pss.2013.06.025.
- 1094 J. B. Pollack, J. M. Schwartz, and K. Rages. Scatterers in Triton's atmosphere
1095 - Implications for the seasonal volatile cycle. *Science*, 250:440–443, October
1096 1990. doi: 10.1126/science.250.4979.440.
- 1097 K. Rages and J. B. Pollack. Voyager imaging of Triton's clouds and hazes.
1098 *Icarus*, 99:289–301, October 1992. doi: 10.1016/0019-1035(92)90147-Y.
- 1099 P. Rannou, M. Cabane, and E. Chassefiere. Growth of aerosols in Ti-
1100 tan's atmosphere and related time scales - A stochastic approach. *Geo-*
1101 *phys. Res. Lett.*, 20:967–970, May 1993. doi: 10.1029/93GL00911.
- 1102 P. Rannou, M. Cabane, E. Chassefiere, R. Botet, C. P. McKay, and R. Courtin.
1103 Titan's geometric albedo: Role of the fractal structure of the aerosols. *Icarus*,
1104 118:355–372, December 1995. doi: 10.1006/icar.1995.1196.

- 1105 P. Rannou, M. Cabane, R. Botet, and E. Chassefière. A new interpretation
1106 of scattered light measurements at Titan's limb. *J. Geophys. Res.*, 102:
1107 10997–11014, 1997. doi: 10.1029/97JE00719.
- 1108 P. Rannou, F. Hourdin, and C. P. McKay. A wind origin for Titan's haze
1109 structure. *Nature*, 418:853–856, August 2002.
- 1110 P. Rannou, C. P. McKay, and R. D. Lorenz. A model of Titan's haze of
1111 fractal aerosols constrained by multiple observations. *Planet. Space Sci.*,
1112 51:963–976, December 2003. doi: 10.1016/j.pss.2003.05.008.
- 1113 P. Rannou, T. Cours, S. Le Mouélic, S. Rodriguez, C. Sotin, P. Drossart,
1114 and R. Brown. Titan haze distribution and optical properties retrieved
1115 from recent observations. *Icarus*, 208:850–867, August 2010. doi: 10.1016/
1116 j.icarus.2010.03.016.
- 1117 W. B. Rossow. Cloud microphysics - Analysis of the clouds of Earth,
1118 Venus, Mars, and Jupiter. *Icarus*, 36:1–50, October 1978. doi: 10.1016/
1119 0019-1035(78)90072-6.
- 1120 D. E. Shemansky, A. I. F. Stewart, R. A. West, L. W. Esposito, J. T. Hallett,
1121 and X. Liu. The Cassini UVIS Stellar Probe of the Titan Atmosphere.
1122 *Science*, 308:978–982, May 2005. doi: 10.1126/science.1111790.
- 1123 E. C. Sittler, R. E. Hartle, R. E. Johnson, J. F. Cooper, A. S. Lipatov,
1124 C. Bertucci, A. J. Coates, K. Szego, M. Shappirio, D. G. Simpson, and
1125 J.-E. Wahlund. Saturn's magnetospheric interaction with Titan as defined
1126 by Cassini encounters T9 and T18: New results. *Planet. Space Sci.*, 58:
1127 327–350, February 2010. doi: 10.1016/j.pss.2009.09.017.
- 1128 B. A. Smith, L. A. Soderblom, D. Banfield, C. Barnet, R. F. Beebe, A. T.
1129 Bazilevskii, K. Bollinger, J. M. Boyce, G. A. Briggs, and A. Brahic. Voyager
1130 2 at Neptune - Imaging science results. *Science*, 246:1422–1449, December
1131 1989. doi: 10.1126/science.246.4936.1422.

- 1132 C. Sotin, K. J. Lawrence, B. Reinhardt, J. W. Barnes, R. H. Brown, A. G.
1133 Hayes, S. Le Mouélic, S. Rodriguez, J. M. Soderblom, L. A. Soderblom,
1134 K. H. Baines, B. J. Buratti, R. N. Clark, R. Jaumann, P. D. Nicholson, and
1135 K. Stephan. Observations of Titan's Northern lakes at 5 μm : Implications
1136 for the organic cycle and geology. *Icarus*, 221:768–786, November 2012. doi:
1137 10.1016/j.icarus.2012.08.017.
- 1138 J. A. Stansberry, J. I. Lunine, and M. G. Tomasko. Upper limits on possible
1139 photochemical hazes on Pluto. *Geophys. Res. Lett.*, 16:1221–1224, Novem-
1140 ber 1989. doi: 10.1029/GL016i011p01221.
- 1141 S. A. Stern, F. Bagenal, K. Ennico, G. R. Gladstone, W. M. Grundy, W. B.
1142 McKinnon, J. M. Moore, C. B. Olkin, J. R. Spencer, H. A. Weaver, L. A.
1143 Young, T. Andert, J. Andrews, M. Banks, B. Bauer, J. Bauman, O. S.
1144 Barnouin, P. Bedini, K. Beisser, R. A. Beyer, S. Bhaskaran, R. P. Binzel,
1145 E. Birath, M. Bird, D. J. Bogan, A. Bowman, V. J. Bray, M. Brozovic,
1146 C. Bryan, M. R. Buckley, M. W. Buie, B. J. Buratti, S. S. Bushman, A. Cal-
1147 loway, B. Carcich, A. F. Cheng, S. Conard, C. A. Conrad, J. C. Cook, D. P.
1148 Cruikshank, O. S. Custodio, C. M. Dalle Ore, C. Deboy, Z. J. B. Dischner,
1149 P. Dumont, A. M. Earle, H. A. Elliott, J. Ercol, C. M. Ernst, T. Finley, S. H.
1150 Flanigan, G. Fountain, M. J. Freeze, T. Greathouse, J. L. Green, Y. Guo,
1151 M. Hahn, D. P. Hamilton, S. A. Hamilton, J. Hanley, A. Harch, H. M.
1152 Hart, C. B. Hersman, A. Hill, M. E. Hill, D. P. Hinson, M. E. Holdridge,
1153 M. Horanyi, A. D. Howard, C. J. A. Howett, C. Jackman, R. A. Jacobson,
1154 D. E. Jennings, J. A. Kammer, H. K. Kang, D. E. Kaufmann, P. Koll-
1155 mann, S. M. Krimigis, D. Kusnierkiewicz, T. R. Lauer, J. E. Lee, K. L.
1156 Lindstrom, I. R. Linscott, C. M. Lisse, A. W. Lunsford, V. A. Mallder,
1157 N. Martin, D. J. McComas, R. L. McNutt, D. Mehoke, T. Mehoke, E. D.
1158 Melin, M. Mutchler, D. Nelson, F. Nimmo, J. I. Nunez, A. Ocampo, W. M.

- 1159 Owen, M. Paetzold, B. Page, A. H. Parker, J. W. Parker, F. Pelletier, J. Pe-
1160 terson, N. Pinkine, M. Piquette, S. B. Porter, S. Protopapa, J. Redfern, H. J.
1161 Reitsema, D. C. Reuter, J. H. Roberts, S. J. Robbins, G. Rogers, D. Rose,
1162 K. Runyon, K. D. Retherford, M. G. Ryschkewitsch, P. Schenk, E. Schind-
1163 helm, B. Sepan, M. R. Showalter, K. N. Singer, M. Soluri, D. Stanbridge,
1164 A. J. Steffl, D. F. Strobel, T. Stryk, M. E. Summers, J. R. Szalay, M. Tap-
1165 pley, A. Taylor, H. Taylor, H. B. Throop, C. C. C. Tsang, G. L. Tyler,
1166 O. M. Umurhan, A. J. Verbiscer, M. H. Versteeg, M. Vincent, R. Webbert,
1167 S. Weidner, G. E. Weigle, O. L. White, K. Whittenburg, B. G. Williams,
1168 K. Williams, S. Williams, W. W. Woods, A. M. Zangari, and E. Zirnstein.
1169 The Pluto system: Initial results from its exploration by New Horizons.
1170 *Science*, 350:aad1815, October 2015. doi: 10.1126/science.aad1815.
- 1171 D. F. Strobel and M. E. Summers. Triton's upper atmosphere and ionosphere.
1172 In D. P. Cruikshank, M. S. Matthews, and A. M. Schumann, editors, *Nep-*
1173 *tune and Triton*, pages 1107–1148, 1995.
- 1174 D. F. Strobel, M. E. Summers, F. Herbert, and B. R. Sandel. The photo-
1175 chemistry of methane in the atmosphere of Triton. *Geophys. Res. Lett.*, 17:
1176 1729–1732, September 1990. doi: 10.1029/GL017i010p01729.
- 1177 C. Szopa, G. Cernogora, L. Boufendi, J. J. Correia, and P. Coll. PAM-
1178 PRE: A dusty plasma experiment for Titan's tholins production and study.
1179 *Planet. Space Sci.*, 54:394–404, April 2006. doi: 10.1016/j.pss.2005.12.012.
- 1180 N. A. Teanby, P. G. J. Irwin, C. A. Nixon, R. de Kok, S. Vinatier, A. Coustenis,
1181 E. Sefton-Nash, S. B. Calcutt, and F. M. Flasar. Active upper-atmosphere
1182 chemistry and dynamics from polar circulation reversal on Titan. *Nature*,
1183 491:732–735, November 2012. doi: 10.1038/nature11611.
- 1184 M. G. Tomasko, B. Archinal, T. Becker, B. Bézard, M. Bushroe, M. Combes,
1185 D. Cook, A. Coustenis, C. de Bergh, L. E. Dafoe, L. Doose, S. Douté,

- 1186 A. Eibl, S. Engel, F. Gliem, B. Grieger, K. Holso, E. Howington-Kraus,
1187 E. Karkoschka, H. U. Keller, R. Kirk, R. Kramm, M. Küppers, P. Lanagan,
1188 E. Lellouch, M. Lemmon, J. Lunine, E. McFarlane, J. Moores, G. M. Prout,
1189 B. Rizk, M. Rosiek, P. Rueffer, S. E. Schröder, B. Schmitt, C. See, P. Smith,
1190 L. Soderblom, N. Thomas, and R. West. Rain, winds and haze during the
1191 Huygens probe's descent to Titan's surface. *Nature*, 438:765–778, December
1192 2005. doi: 10.1038/nature04126.
- 1193 O. B. Toon, C. P. McKay, C. A. Griffith, and R. P. Turco. A phys-
1194 ical model of Titan's aerosols. *Icarus*, 95:24–53, January 1992. doi:
1195 10.1016/0019-1035(92)90188-D.
- 1196 M. G. Trainer, A. A. Pavlov, H. L. Dewitt, J. L. Jimenez, C. P. McKay,
1197 O. B. Toon, and M. A. Tolbert. Inaugural Article: Organic haze on Titan
1198 and the early Earth. *Proceedings of the National Academy of Science*, 103:
1199 18035–18042, November 2006. doi: 10.1073/pnas.0608561103.
- 1200 B. N. Tran, M. Force, R. G. Briggs, J. P. Ferris, P. Persans, and J. J. Chera.
1201 Titan's atmospheric chemistry: Photolysis of gas mixtures containing hydro-
1202 gen cyanide and carbon monoxide at 185 and 254 nm. *Icarus*, 193:224–232,
1203 January 2008. doi: 10.1016/j.icarus.2007.09.010.
- 1204 J. H. Waite, H. Niemann, R. V. Yelle, W. T. Kasprzak, T. E. Cravens, J. G.
1205 Luhmann, R. L. McNutt, W.-H. Ip, D. Gell, V. De La Haye, I. Müller-
1206 Wordag, B. Magee, N. Borggren, S. Ledvina, G. Fletcher, E. Walter,
1207 R. Miller, S. Scherer, R. Thorpe, J. Xu, B. Block, and K. Arnett. Ion
1208 Neutral Mass Spectrometer Results from the First Flyby of Titan. *Science*,
1209 308:982–986, May 2005. doi: 10.1126/science.1110652.
- 1210 J. H. Waite, D. T. Young, T. E. Cravens, A. J. Coates, F. J. Crary, B. Magee,
1211 and J. Westlake. The Process of Tholin Formation in Titan's Upper Atmo-
1212 sphere. *Science*, 316:870–, May 2007. doi: 10.1126/science.1139727.

- 1213 R. A. West and P. H. Smith. Evidence for aggregate particles in the at-
1214 mospheres of Titan and Jupiter. *Icarus*, 90:330–333, April 1991. doi:
1215 10.1016/0019-1035(91)90113-8.
- 1216 E. H. Wilson and S. K. Atreya. Chemical sources of haze formation in Titan’s
1217 atmosphere. *Planet. Space Sci.*, 51:1017–1033, December 2003. doi: 10.
1218 1016/j.pss.2003.06.003.
- 1219 E. H. Wilson and S. K. Atreya. Current state of modeling the pho-
1220 tochemistry of Titan’s mutually dependent atmosphere and ionosphere.
1221 *Journal of Geophysical Research (Planets)*, 109:E06002, June 2004. doi:
1222 10.1029/2003JE002181.
- 1223 R. V. Yelle, N. Borggren, V. de la Haye, W. T. Kasprzak, H. B. Niemann,
1224 I. Müller-Wodarg, and J. H. Waite. The vertical structure of Titan’s upper
1225 atmosphere from Cassini Ion Neutral Mass Spectrometer measurements.
1226 *Icarus*, 182:567–576, June 2006. doi: 10.1016/j.icarus.2005.10.029.
- 1227 A. Zangari. A meta-analysis of coordinate systems and bibliography of their
1228 use on Pluto from Charon’s discovery to the present day. *Icarus*, 246:93–145,
1229 January 2015. doi: 10.1016/j.icarus.2014.10.040.